ADVANCED FUNCTIONAL MATERIALS
www.afm-journal.de

Enhanced Direct Air Carbon Capture on NaX Zeolite by Electric-Field Enhanced Physical Adsorption and In Situ CO_2 Synergistic Effects of Cold Plasma

Minghai Shen, Fulin Kong, Wei Guo, Zhongqi Zuo, Chan Guo, Lige Tong, Shaowu Yin, Li Wang, Sibudjing Kawi,* Paul K. Chu,* and Yulong Ding**

Direct air carbon capture (DAC) is vital to achieving negative CO_2 emissions, with physical adsorption offering a cost-effective and energy-efficient solution. an advanced zeolite modification technique is presented using cold plasma, which enhances the CO_2 adsorption efficiency of NaX zeolite by 11.5% after just 60 min. This method utilizes the electric field to reorganize cation distribution and pore structure and significantly improve the adsorption capacity, efficiency, and selectivity. Compared to traditional methods, this technique is simpler and more effective, as demonstrated through first-principles calculations, thermodynamics, kinetics, and adsorption equilibrium studies.

1. Introduction

Carbon dioxide is one of the greenhouse gases contributing to global warming and countries around the world are striving to achieve carbon neutrality, that is, balancing the emissions by capturing and storing carbon dioxide.[1] Direct air carbon capture techniques enable the capture of carbon dioxide from the atmosphere to mitigate carbon emissions and reduce the concentration of carbon dioxide in the atmosphere.[2,3] However, direct air carbon capture is challenging as it involves multiple issues, such as the development of efficient adsorption materials, energy consumption, and economic feasibility.[4,5]

Commercial DAC systems usually use solid organic amine adsorbents in which the amine groups are physically or chemically combined with porous carriers such as activated carbon, molecular sieves, porous nanomaterials, and reactive oxidants.[6,7] Combining the advantages of large specific surface area, high physical selectivity, and high capacity of the amine functional groups in porous adsorbents, chemical absorption for carbon capture has prospects for low carbon dioxide concentrations (≈400 ppm) and in humidity-resistant environments.[8,9] However, these chemical adsorbents require an elevated temperature (>100 °C) for regeneration. In high-temperature or high-pressure environments for regeneration, external water vapor and accumulation in the adsorption bed can lead to failure of the amine functional groups in the chemical adsorbents. The disadvantages of physical adsorption include weak adsorption strength, poor selectivity, limited adsorption capacity, sensitivity to environmental conditions such as temperature and humidity, and a significant decrease in adsorption at high temperatures. In addition, although regeneration is relatively easy, it still requires a certain amount of energy, may cause performance degradation during long-term use, and has a slow adsorption rate, which limits its application in large-scale rapid processing.

Although physical adsorption and chemical adsorption have their own advantages and disadvantages, in many application scenarios, physical adsorption has become an important choice in carbon capture technology due to its advantages such as low energy consumption, good regeneration performance, stable materials, environmental friendliness, and simple operation. Especially in scenarios that require frequent regeneration and long-term use, the advantages of physical adsorption are more obvious. Therefore, compared with chemical adsorbents, physical adsorption is more economical and practical for commercial applications.[10]

M. Shen, F. Kong, W. Guo, Z. Zuo, L. Tong, S. Yin, L. Wang
Beijing Key Laboratory of Energy Saving and Emission Reduction for Metallurgical Industry
School of Energy and Environmental Engineering
University of Science and Technology Beijing
Beijing 100083, China
E-mail: tonglige@me.ustb.edu.cn

M. Shen, S. Kawi
Department of Chemical and Biomolecular Engineering
National University of Singapore
Singapore 119260, Singapore
E-mail: chekawis@nus.edu.sg

C. Guo
101 Research Institute of the Ministry of Civil Affairs
Beijing 100070, China

P. K. Chu
Department of Physics
Department of Materials Science and Engineering, and Department of Biomedical Engineering
City University of Hong Kong
Kowloon, Hong Kong 999077, China
E-mail: paul.chu@cityu.edu.hk

Y. Ding
Birmingham Centre for Energy Storage & School of Chemical Engineering
University of Birmingham
Birmingham B15 2TT, UK
E-mail: Y.Ding@bham.ac.uk

The ORCID identification number(s) for the author(s) of this article can be found under https://doi.org/10.1002/adfm.202408922

DOI: 10.1002/adfm.202408922

Among the various physical adsorbents, zeolite, a crystalline aluminosilicate microporous substance, is used commercially in catalysis, adsorption, and separation.[11] Zeolite adsorbents based on physical adsorption have high selectivity and adsorption capacity, adjustability, excellent regeneration performance, and multifunctional applications. Moreover, they can be used for direct air carbon capture under harsh conditions.[12] Carbon dioxide adsorbs physically on zeolite via van der Waals and electrostatic forces at a low temperature, and the optimized porous structure can be utilized for selective carbon dioxide capture.[13,14] The screening effects generated by the restricted pores in the zeolite and cation exchange sites in the pores can adjust the carbon dioxide adsorption selectivity in different environments.[15] However, the complex preparation processes and unstable porous structures are challenging for carbon dioxide capture applications.[16] Compared to synthesis of bulk materials, post-processing such as ion exchange[17] and alternation of the crystal field strength,[18] acidity, and alkalinity[19] can produce excellent properties in certain environments.

The non-thermodynamic equilibrium discharge characteristics of cold plasma can enable thermodynamically and kinetically infeasible chemical reactions to occur. A certain intensity of electric field and high-energy particles is generated between the electrodes, which can be used to process and synthesize materials. Electrons produced by cold plasma can be accelerated by an external electric field, resulting in higher electron temperatures (10000–250000 K) and typical electron energies (1–25 eV). This energy is enough to break most chemical bonds, such as the decomposition and recombination of gases. As a physical field, the electric field affects the adsorption/desorption of zeolite, so it was usually used as a means equivalent to temperature swing/pressure swing adsorption.[20,21] Electric fields can also cause changes in the charge distribution inside the material, thereby changing the surface energy and surface chemical properties of the material and promoting the adsorption of specific ions or molecules.[22] Second, the electric field may cause the rearrangement or deformation of the pores and pore sizes in the material, optimizing the pore structure to enhance the transmission and diffusion performance of gas molecules.[23,24] Electric field-induced ion migration and interfacial effects can improve the conductivity and stability of the material, and further improve its adsorption and catalytic properties. These mechanisms work together to make the electric field an effective means of regulating the structure and properties of porous materials.[25,26]

The channel limitation and cation distribution may enhance the CO_2 adsorption/separation capacity in the gas mixture in a certain range. However, there have been no concrete studies to prove whether the positive effect of E-field is only valid for CO_2 in the presence of water vapor, which competes for a stronger adsorption capacity in DAC.

Compared to the relatively mature high-concentration CO_2 adsorption technology, low-concentration CO_2 separation demands materials with extremely high selectivity to efficiently separate CO_2 from other gases like nitrogen and oxygen. With an atmospheric CO_2 concentration of ≈0.04%, these materials must effectively adsorb CO_2 without interference from other gases, such as water vapor. Additionally, they need high adsorption capacity and rapid response at low pressure to enhance separation efficiency.[27,28] Inspired by cold plasma processing of other materials, we developed an efficient material modification technology for DAC. Based on the advantage of cold plasma in modifying the material surface without changing the overall properties of the material, the adsorption capacity and adsorption selectivity of zeolite materials can be improved by adjusting electronic properties and manipulating local structural changes.

In this work, NaX zeolite is selected as the physical adsorbent because it can capture more than 99.99% of CO_2 and H_2O from air.[29] In addition, commercial NaX zeolite has a long storage life and service life, in addition to hydrothermal stability.[30] A cold plasma formed by a dielectric barrier discharge (DBD) is adopted in combination with a CO_2 environment to control the porous structure of the NaX zeolite. The structure of the NaX zeolite O-T-O (T = Si, Al) is modified by steric hindrance, as shown in **Figure 1**. The DBD treatment in CO_2 not only improves the surface area of the NaX zeolite, but also mitigates the negative effects of H_2O on CO_2 adsorption by enhancing selective adsorption of CO_2 by O-Si-O. After the treatment for 60 min (PC60-NaX), the CO_2 adsorption efficiency increases by 11.5%, reaching 5.49 mmol g^{-1}.

2. Results and Discussion

2.1. Preparation and Characterization of PC60-NaX Zeolite

CO_2 can be converted into CO_2^* species in the forms such as CO_2^+, CO_2^{2+}, C^+, O^+, and others by electron activation.[31] These chemically active CO_2^* species have lower adsorption energy and Gibbs free energy, and can react with metal oxides to form carbonates.[32] Although both CO_2 and SiO_2 are group IV oxides, they have different bonding properties and phase behavior under ambient conditions. Solid silicon carbonate is typically prepared by the reaction of CO_2 and SiO_2 at high pressure[33] and therefore, converting the O-T-O (T = Si, Al) skeleton in the NaX zeolite into a carbonate structure requires high energy and pressure. Electron bombardment can alter the material structure,[34] while energetic ion bombardment modifies the material surface through processes such as ion mixing, sputtering, compound formation, defect formation, and ion implantation.[35] Consequently, structural changes, including bond lengths, bond angles, and bonding energy, can result in deeper structural changes requiring a higher energy and longer time.[36] We create an in situ plasma environment through CO_2 and our custom-made, specifically DBD equipment. We treat NaX zeolite with the electric field produced between the various DBD electrodes and the in situ plasma gas to generate a range of NaX zeolites treated under different conditions. Figure S1 (Supporting Information) shows the series of NaX zeolites (PC30-NaX, PC60-NaX, PC90-NaX, PC120-NaX, and PC180-NaX) treated for different time durations in our experiments.

The microstructures of NaX zeolite at different scales before and after treatment were analyzed by Scanning Electron Microscope (SEM), Transmission Electron Microscope (TEM) and Energy Dispersive Spectroscopy (EDS) techniques to determine the effect of cold plasma coupled in situ CO_2 on the material surface. The in situ plasma CO_2 treatment does not change the morphology and crystal phase of the NaX zeolite, as shown in **Figure 2**a,b, and the effect is further illustrated in Figure 2c,d. Due to the influence of the E-field strength, frequency, and time, there are some

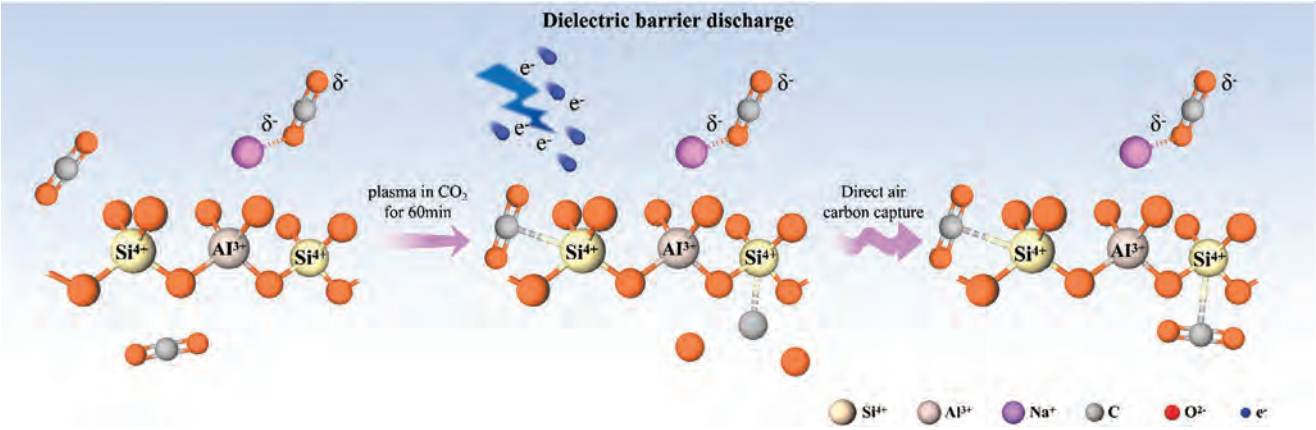

Figure 1. Schematic diagram of the modification of the NaX zeolite by the DBD in the CO_2 atmosphere. In general, CO_2 molecules do not affect the structure of NaX zeolite (left), but exposure to in situ CO_2 generated by cold plasma for 60 min modifies the zeolite pore structure and cation distribution (middle). The treated NaX zeolite exhibits excellent performance in direct air carbon capture applications (right).

changes on the surface of NaX after the 200 kV m^{-1} treatment for 60 min. XRD showed that the crystal structure did not change under this cold plasma electric field treatment (Figure S2, Supporting Information). Different forms of CO_2^* exist on the NaX zeolite after activation, but EDS reveals uniform distributions of Na, Al, Si, and O on the surface. A trace amount of C was observed from Figure 2e and it may be deposited/loaded on the NaX zeolite in the form of C^+ or carbonate. The BET technique is used to further explore the changes in the specific surface area and internal pore structure of NaX zeolite. Table S1 and Figure S3a–d (Supporting Information) show the properties of NaX zeolite after different treatments revealing larger surface areas. The adsorption of N_2 by PC60-NaX at 77 K increases significantly, and the BET surface area increases from 539.01 to 628.63 m^2 g^{-1}. As

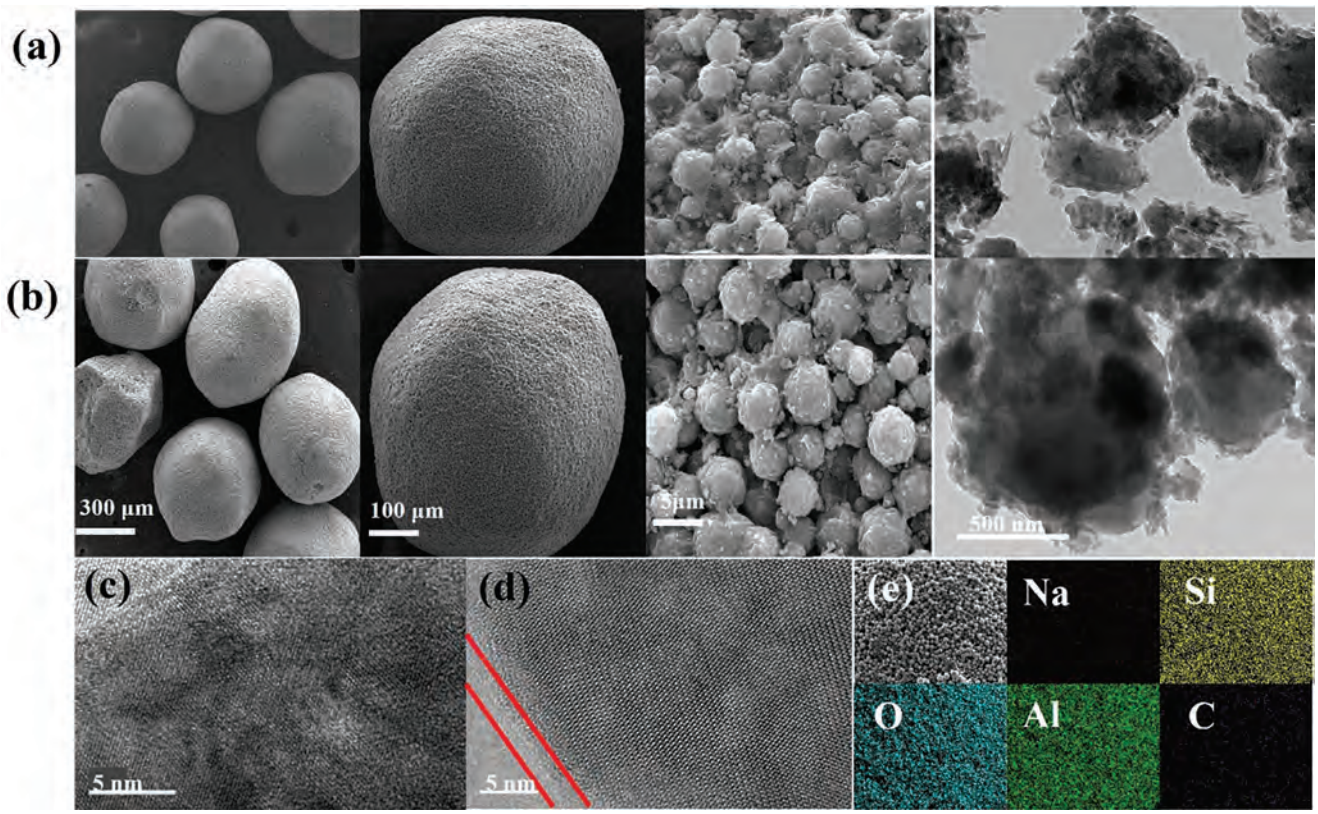

Figure 2. SEM images of the NaX zeolite at different magnifications before a) and after b) the in situ plasma CO_2 treatment; TEM images of c) Pristine NaX zeolite and d) Processed NaX zeolite at high magnification; e) EDS elemental maps of the NaX zeolite after the plasma treatment.

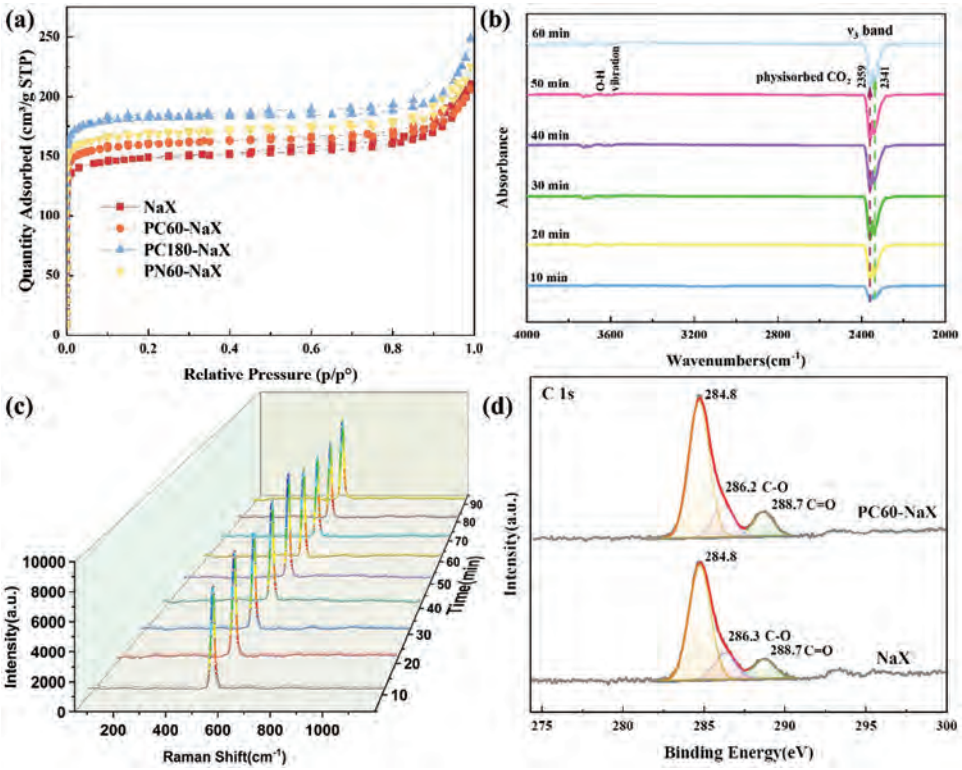

Figure 3. a) N_2 adsorption isotherms of NaX, PC60-NaX, PC180-NaX, and PN60-NaX zeolites; b) In situ infrared spectra of PC60-NaX for different adsorption times in the CO_2 atmosphere; c) In situ UV-Raman spectra of NaX at different times; d) High-resolution C 1s spectra of XPS spectra of NaX and PC60-NaX.

the treatment time increases, the pore diameter and pore volume increase. Since there are pores of different sizes in the NaX zeolite, there are mesopores with more CO_2^* as well as micropores. In general, the larger the surface area, the more extensive surface adsorption.[37] As the surface area increases, the number of adsorbed molecules also increases. As shown in **Figure 3a**, all the NaX samples exhibit the type I isotherms, and adsorption increases rapidly at a low relative pressure, consistent with microporous adsorption of zeolite molecular sieves.[38]

To elucidate the mechanism for enhanced adsorption of the modified NaX zeolite, the CO_2 adsorption sites in different stages during the plasma CO_2 treatment for 60 min are monitored by in situ infrared spectroscopy. As shown in Figure 3b and Figure S4a,b (Supporting Information), as time increases, peaks appear at 2341 and 2359 cm^{-1}. The physical absorption band of CO_2 usually appears in the range of 2350–2370 cm^{-1} as the $\nu 3$ band. The fine structure of the CO_2 bands may reflect the adsorption of CO_2 at different positions, and usually, this fine structure only appears for absorption at high concentrations of CO_2 ($\geq$ 3.73% v/v, Figure S4c, Supporting Information) by NaX. As the CO_2 adsorption time increases, there is no obvious strong absorption peak due to chemical adsorption for the $\nu 2$ band (1200–1700 cm^{-1}), suggesting that the higher adsorption capacity of the modified PC60-NaX zeolite is caused by the increased physical adsorption capacity for CO_2.

The vibration of cyclic elements (four-, six-, and other-membered rings, etc.) in the zeolite structure may be detected by Raman spectroscopy. Finding the alterations in the zeolite crystal structure is highly beneficial. We adopt cold plasma technology in a CO_2 environment to perform in situ Raman spectroscopy characterization of the original NaX solid sample at various time scales. Figure 3c is the in situ UV Raman spectrum of the NaX sample. The 200–600 cm^{-1} region in the figure is related to the ring structure unit of the zeolite. The sharp peak at 535 cm^{-1} is the bending vibration peak of the four-ring TO_4 (T = Si, Al), and 290 and 375 cm^{-1} are the bending vibration peaks of the six-membered ring. They are all characteristic peaks of NaX zeolite.[39] The small peak at 813 cm^{-1} can be attributed to the symmetric stretching vibration of T—O, and the two broader peaks at 1000 and 1074 cm^{-1} can be attributed to the asymmetric stretching vibration of T—O. With the increase in reaction time, the peak intensity corresponding to the characteristic peak gradually changes.[40] The peak intensity of 535 cm^{-1} is the lowest at 60 min, and a small peak emerges at 731 cm^{-1}. These prove that the framework structure of NaX zeolite partially collapses or reconstructs, thus affecting the characteristic peaks in the Raman spectrum.

The XPS survey spectra reveal uniform distributions of Na, Al, Si, and O in NaX and PC60-NaX. The Al *2p*, Si *2p*, and O *1s* spectra indicate that the external E-field does not affect the chemical states of O-T-O (T = Si, Al) (Figure S5a–d, Supporting Information). The C *1s* peaks at 284.8, 286.3, and 288.7 eV correspond to C—C, C—O, and C=O, respectively (Figure 3d). The XPS and FTIR results are basically consistent, and the C-O peak of PC60-NaX shifts on account of adsorbed CO_2 from the surroundings.

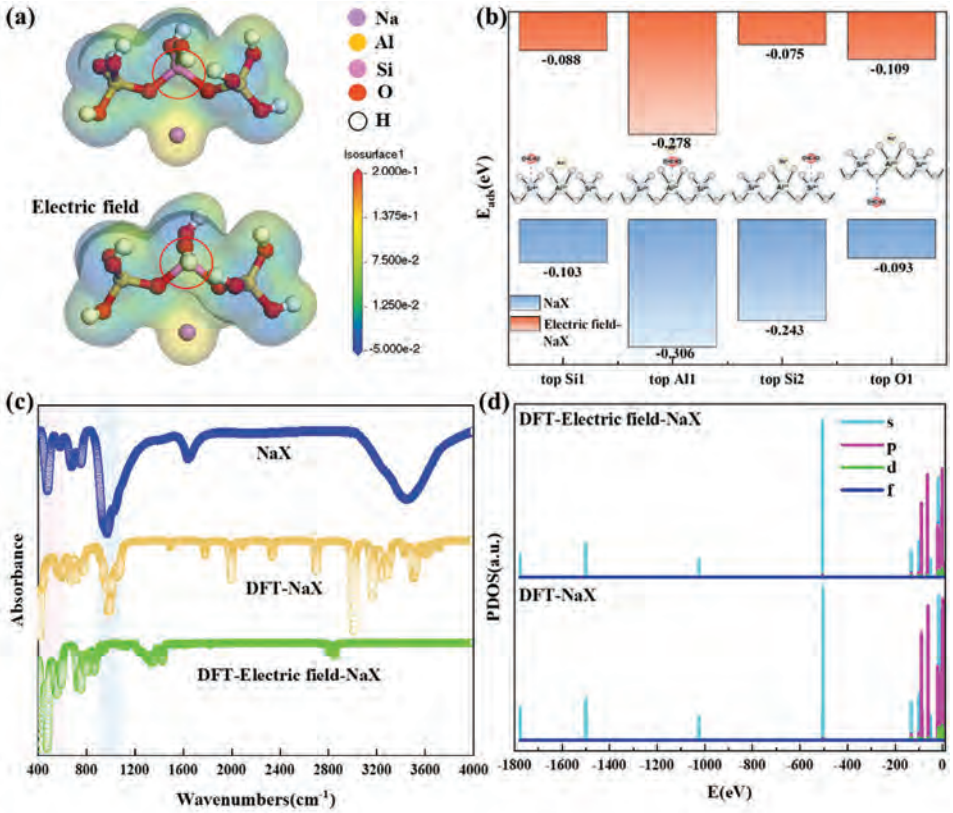

Figure 4. a) Surface electrostatic potential energies of the O-T-O (T = Al, Si) skeleton without E-field and plasma treatment; b) Adsorption energies of different adsorption sites simulated by DFT (Table S3, Supporting Information); c) Infrared spectra of the NaX samples and the NaX twelve-membered ring without the E-field simulated by DFT; d) Partial wave density of states of the NaX twelve-membered ring without the E-field by DFT simulation.

The affinity of zeolites for specific gases can be attributed to the polarizability of the adsorbed molecules, and a larger quadrupole moment of the adsorbate produces stronger interactions with the E-field generated by the zeolite cations.[41] Adsorption of CO_2 on the zeolite mainly stems from the ion-dipole interactions with polarized CO_2 interacting with the cations in the zeolite pores. Moreover, under the action of the external E-field, the force between CO_2 and NaX zeolite (attraction and repulsion by van der Waals force) weakens, and hence, the dual effects of CO_2 exposure and the plasma alter the structure and surface properties of the NaX zeolite. The interaction potential between gas and porous material is bound to be affected by the polarization of applied E-field during DBD operation,[42] which changes the adsorption capacity. In order to fully study the adsorption performance of carbon dioxide by zeolite under the action of multiple physical fields, the E-field action should also be analyzed.

2.2. Mechanism of E Field-Regulated O-T-O (T = Al, Si) Skeleton

According to the structure of the NaX zeolite, a silica-aluminum zeolite molecular sieve skeleton composed of the Si-O tetrahedron and Al-O tetrahedron, namely O-T-O (T = Al, Si), is established. The effects of CO_2 and the E-field are investigated by first-principles calculation based on the density-functional theory (DFT). As shown in Table S2 (Supporting Information), when the O-T-O (T = Al, Si) skeleton is adsorbed or surrounded by CO_2, the bond length and bond angle change slightly due to steric hindrance. The 200 kV m^{-1} E-field consistent with the power of the DBD system also fine tunes the O-T-O (T = Al, Si) skeleton. In the presence of both the E-field and CO_2, the skeleton changes. For example, O-Al-O shows the largest angle change. **Figure 4a** shows the surface electrostatic potential energy distributions under the external E-field. Since the surface electrostatic potential energy increases, the distance between Al_1 and Na^+ becomes larger, so that CO_2 molecules that originally adsorb around Na^+ have a chance to adsorb on the Al_1 atoms. The CO_2^* and electric field changes under plasma activation cause the O-T-O (T = Al, Si) skeleton to vibrate and change. More micropores or mesopores may be created, thereby increasing the specific surface area. However, this structural adjustment causes part of the original larger pores to be blocked or reduced, resulting in a reduction in the average pore size (Table S1 and Figure S3a–d, Supporting Information).

The pore size and shape of molecular sieves are precisely controlled and optimized through post-processing. For example, the most well-researched type A molecular sieve has an intrinsic pore size of 4.2 Å. However, the pore size can be modulated by the size and charge of the cation, varying between 3.0 and 5.0 Å. Among them, the pore diameter of K-A (3A) is 3.0 Å, the pore diameter

of Na-A (4A) is 3.8 Å, and the pore diameter of Ca-A (5A) is 4.8 Å.

The adsorption and desorption behavior of CO_2 on the surface of NaX zeolite has essentially the molecular scale. Therefore, in order to reveal the effects of the applied E-field on the adsorption of carbon dioxide by NaX zeolite, it is necessary to simulate the Dmol3 module using the density-functional theory on the microscopic level. Because of the need to examine changes in the electron density, the gradient approximation functional is chosen (see Experimental Section for detailed simulation methods).

Figure 4b presents the adsorption energies of CO_2 at different positions on the O-T-O (T = Al, Si) skeleton simulated by DFT (only the top position of the atom is considered). In the absence of an E-field, CO_2 located between Al_1 and Na^+ has larger adsorption energy (−0.306 eV) due to the electrostatic and acid-base interactions between Na^+ and CO_2. In a low-concentration CO_2 environment, more CO_2 molecules preferentially approach and adsorb at Na^+, while other sites do not capture CO_2 due to the smaller adsorption energy and restricted spatial structure. However, in the presence of an E-field, the adsorption energies on Al_1, Si_1, and Si_2 decrease. The adsorption energy of O_1 increases from −0.093 to −0.109 eV, which is in line with the surface electrostatic potential energy distribution due to changes in the O-T-O (T = Al, Si) skeleton. The angle of O-Al-O increases, and the charge distribution is skewed to O on both sides. Therefore, the adsorption energy of O_1 increases. Although the adsorption energy of O-T-O (T = Al, Si) decreases, the CO_2 adsorption capacity of the NaX zeolite can be increased by optimizing the surface of the NaX twelve-membered ring.

Considering that NaX is a twelve-member ring structure composed of multiple O-T-O (T = Al, Si) skeletons, the structural changes are more complex than those of the single O-T-O (T = Al, Si) due to interactions among the skeletons. As shown in Figure 4c, the twelve-member ring after E-field optimization retains the characteristic peaks of NaX zeolite (400–1000 cm^{-1}).[43] Since H is used to seal the edge of the twelve-member ring, some impurity peaks are observed from the 1500–3500 cm^{-1} range. By comparing the partial wave density of states (PDOS) of the NaX twelve-member ring without and with an external E-field, the E-field does not increase or eliminate the energy levels of the atoms in NaX (Figure 4d). Instead, it reduces the mutual electrostatic potential between atoms by weakening the electron distribution between different orbits, resulting in smaller adsorption energy. This is consistent with the surface electrostatic potential and adsorption energy changes simulated. Therefore, it is believed that the external E-field activates the bonds in the NaX zeolite with low-frequency and high-energy electrons and weakens the interactions between CO_2 and the O-T-O (T = Si, Al) skeleton. Furthermore, owing to steric hindrance, different forms of CO_2^* adsorb and diffuse in the NaX zeolite to change the skeleton with the stable forms coexisting with $CO_2^{*.}$ After the plasma treatment, without an external E-field, the repulsive force between CO_2 and the O-T-O (T = Si, Al) skeleton is restored, and the modified O-T-O (T = Si, Al) skeleton remains stable.

Since the CO_2 molecule has an appropriate volume size and partial negative charge, a stable conformation exists when CO_2 adsorption occurs. Fine-tuning of the pore size and channel structure results in the two terminal O atoms of O = C = O being able to simultaneously interact with the Na^+ ions located in the center of the single 12-member ring and the Na^+ ions located in the single 6-membered ring on the β cage. Precisely because CO_2 can interact with multiple Na+ ions located at different sites at the same time, NaX has a relatively high adsorption capacity for CO_2 even in low-pressure areas.

The O-T-O skeleton in NaX zeolite is stable based on chemical bonds. In order to make up for the vacancies of positive charges, Na+ is fixed at different points based on the charge distribution of the O-T-O skeleton. The forces between these atoms restrain and stabilize each other, thus ensuring the high stability of NaX zeolite. Our previous study on the structural shrinkage and collapse of NaX zeolite at high temperatures is based on the vibration of the O-T-O skeleton.[44] This showed that the introduction of external energy can change the structure of NaX zeolite. Different from the thermal energy evenly dispersed in the environment, the electric field directed from positive charges to negative charges is a vector, so the electric field force generated by it may strengthen/suppress the atomic/ion force between NaX zeolites. In particular, Na+ relies on van der Waals forces and electrostatic potential energy to stabilize it, as shown in **Figure 5**.

The above simulation proves that the surface energy of the O-T-O framework is reduced under the action of the electric field, so CO_2* activated by the electric field can more easily reach the atomic layer surface of NaX zeolite. Based on the direction of the electric field, the movement behavior, such as adsorption/desorption and flow of CO2* between NaX zeolites, is controlled. The low-energy structure of the NaX zeolite skeleton and Na+ are changed by multiple physical fields such as van der Waals force and electrostatic potential energy to quickly pass through and accommodate different types of CO_2*.

2.3. CO_2 Adsorption and Desorption Kinetic Analysis

To evaluate the feasibility of the industrial application of PC60-NaX, we compare it with commercial NaX through kinetic and thermodynamic experiments. In general, the adsorption isotherm refers to the study of the distribution of the two phases when the adsorbent migrates from the water phase to the solid phase at a fixed pH and temperature. Four isothermal adsorption models, Langmuir, Freundlich, Temkin, and Dubinin-Radushkevich, are used to simulate the experimental results. As shown in **Figure 6**a,b, the Langmuir model of untreated NaX shows the best fitting effect (R^2 = 0.99) (Figures S6 and S7 and Table S4, Supporting Information). However, the Freundlich model of PC60-NaX is also relatively good (R^2 = 0.98), followed by the Langmuir model of PC60-NaX (R^2 = 0.97). The results show that the adsorption of CO_2 by PC60-NaX is mainly monolayer adsorption (See Supporting Information for the detailed calculation formula). The surface of the NaX zeolite treated by plasma in situ CO_2 has a certain heterogeneity, and heterogeneous surface structures are formed due to surface deposition of active CO_2^*.

The adsorption kinetics studies disclose the relationship between adsorption capacity and time, which plays an important role in determining the equilibrium time and the optimal contact time required for the adsorption process. In order to reveal the adsorption behavior, the pseudo-first-order kinetic model (PFO) and pseudo-second-order kinetic model (PSO) are used to fit the experimental data. As shown in Figure 6c,d), the adsorption

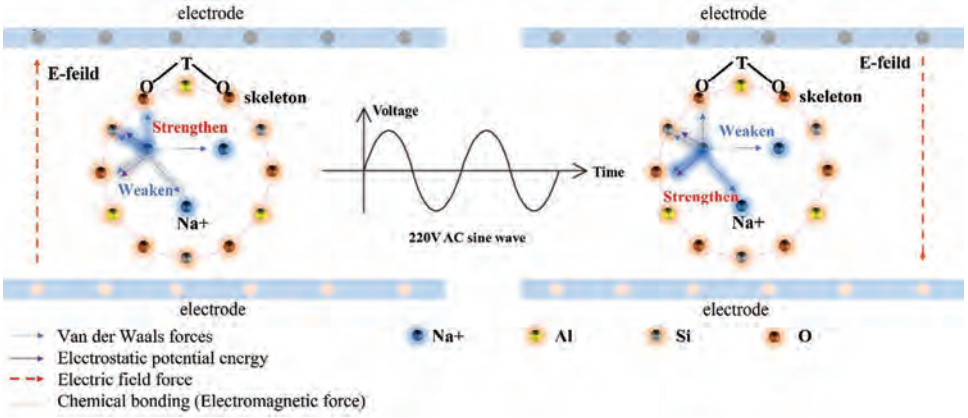

Figure 5. Na+ migration and O-T-O (T = Al, Si) skeleton vibration changes under the coupling effect of multiple physical fields. The high-voltage and ground electrodes create a changing electric field, affecting Na+ adsorption in zeolite. When the electric field aligns with adsorption forces, they strengthen(blue shade); otherwise, they weaken(gray shades). This disrupts Na+ distribution, triggering a chain reaction. High-voltage fields reduce the O-T-O framework's bond energy, causing it to vibrate, reconstruct, or collapse.

capacity q fitted by the pseudo-first-order kinetic model is closer to the experimental results of PC60-NaX at 40 °C (R^2 = 0.93) (Table S5, Supporting Information). The results show that the adsorption of low-concentration CO_2 by PC60-NaX is more consistent with the pseudo-first-order kinetic model, and that of CO_2 by PC60-NaX may be purely physical adsorption. Table S7 (Supporting Information) shows the thermodynamic parameter results, and Figure S8 (Supporting Information) shows the Van' Hoff plot of 1/T at three temperatures. The curve of PC60-NaX is higher than that of NaX, and the corresponding reaction equilibrium constant is larger, that is, the reaction is more favorable at this temperature.

Based on the adsorption isotherm of N_2 by zeolite at 77 and 273 K, the equivalent adsorption heat q_{st} of zeolite is obtained (Figure S9, Supporting Information). q of NaX is 10.60 kJ mol^{-1}, while that of PC60-NaX treated with the CO_2 plasma in situ is

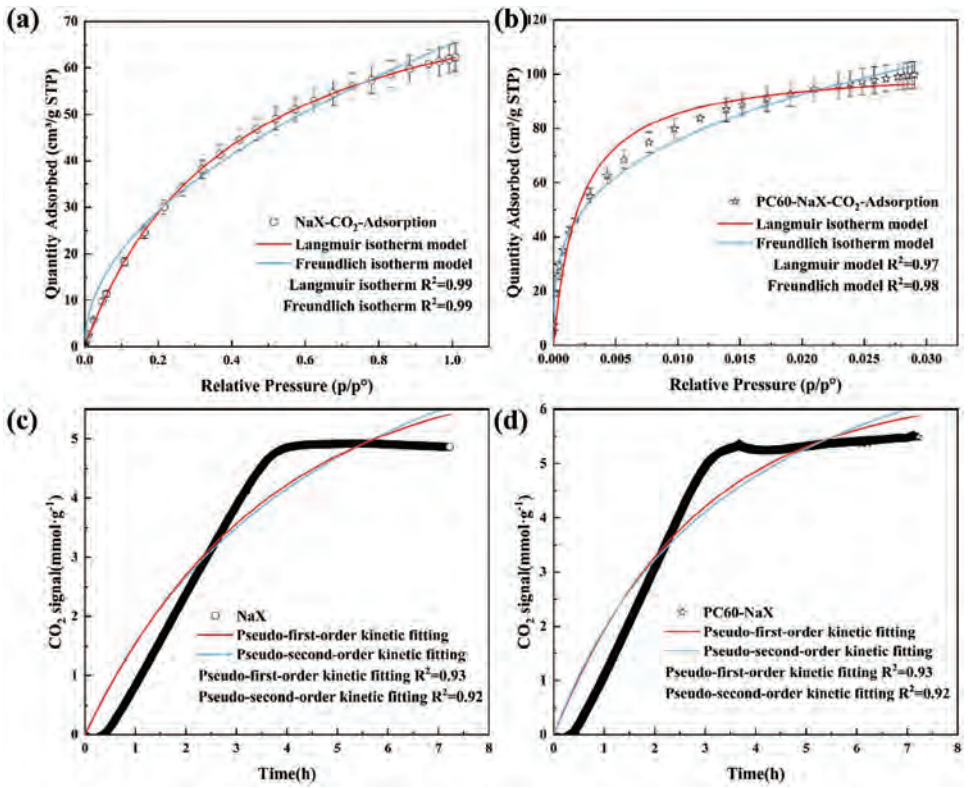

Figure 6. a) isotherm fitting of CO_2 adsorption by NaX; b) isotherm fitting of CO_2 adsorption by PC60-NaX; c) Kinetic model fitting of 400 ppm CO_2 adsorption by NaX; d) Kinetic model fitting of 400 ppm CO_2 adsorption by PC60-NaX.

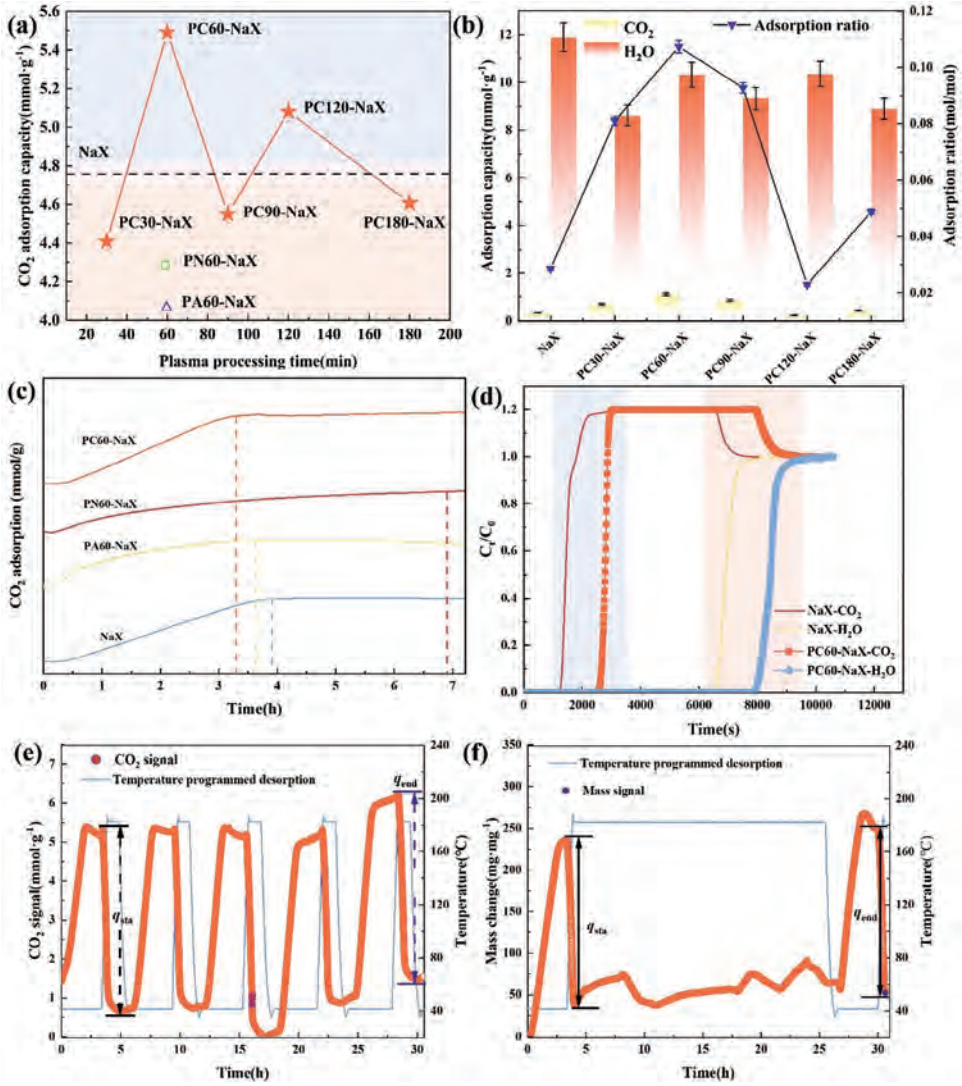

Figure 7. a) Adsorption characteristics of the NaX zeolite after different plasma treatments at a low concentration CO_2; b) Adsorption ratio for different plasma treatment time for RH of 40% and 400 ppm CO_2 in the surroundings; c) Adsorption curves of PC60-NaX, PN60-NaX, PA60-NaX, and NaX at 400 ppm CO_2; d) Multicomponent adsorption-competition curves of CO_2 and H_2O; e) Five consecutive adsorption/desorption cycles of PC60-NaX; f) Stability of PC60-NaX during the continuous 20-h hydrothermal treatment.

12.56 kJ mol^{-1}. This indicates that the adsorption energy of PC60-NaX is stronger and also proves that PC60-NaX is physical adsorption. By absorbing the same amount of N_2, the heat only increases by 18.49%. The 18.49% increase in adsorption heat is a obvious improvement in the field of physical adsorption, especially in adsorption processes based on van der Waals forces. This increase not only shows that the modification effect of the material is significant, but also indicates that it can bring higher adsorption efficiency and economic benefits in practical applications.

2.4. DAC Application Evaluation

To evaluate the carbon capture capacity in air, the sample is exposed to 400 ppm CO_2/N_2 for different time durations, and the CO_2 adsorption characteristics are evaluated by temperature-programmed desorption (TPD). **Figure** 7a shows that PC60-NaX has the maximum adsorption capacity (5.49 mmol g^{-1}). Compared to the untreated sample, the adsorption capacity of PC60-NaX increases by 11.5% (Figure S10a,b, Supporting Information). Furthermore, compared with other physical adsorbents and chemical adsorbents, it has excellent adsorption selectivity for CO_2 under the same conditions (Table S8, Supporting Information). On the contrary, the sample treated with the N_2 and Ar plasmas shows a reduced CO_2 adsorption capacity. Owing to the competitive adsorption of CO_2 and H_2O by the NaX zeolite for different treatment times (Figure 7b), the adsorption capacity of H_2O by PC60-NaX decreases by 13.26%, but that of CO_2 increases by 2.25 times.

By considering the surface electrostatic potential energy distribution simulated by DFT (Figure S11, Supporting Information), the external E-field makes the surface electrostatic potential distribution more polarized, resulting in the separation of the adsorption sites for CO_2 and H_2O and the adsorption ratio of

PC60-NaX for competitive adsorption of CO_2 and H_2O increasing from 0.028 to 0.107 mol mol^{-1}. In the carbon capture process of zeolite, there is competitive adsorption between CO_2 and H_2O, and the mass transfer and adsorption of H_2O is better than that of CO_2. Therefore, H_2O is the heavier component, and the adsorption ratio is calculated by Equation (1):[45]

$$\text{Adsorption ratio} = \frac{x_a}{x_b} \tag{1}$$

where x_a is the molar concentration of the lighter component (CO_2) and x_b is the molar concentration of the more reconstituted component (H_2O).

TPD-TGA experiments are performed for the different plasma treatments. As shown in Figure 7c, compared with the original zeolite, the adsorption rate of PC60-NaX increases by 28.9% from 1.23 to 1.59 mmol g^{-1} h$^{-1,}$ revealing better CO_2 mass transfer. Although the NaX zeolite treated with Ar (60 min) reaches adsorption saturation earlier than the untreated NaX zeolite, the adsorption rates of the Ar (60 min) and N_2 (60 min) treated NaX zeolite are 0.93 and 0.43 mmol g^{-1} h^{-1}, respectively. Figure 7c proves that PC60-NaX has an excellent adsorption saturation rate in humid air.

In the multi-component competitive adsorption experiment, the adsorption capacity of CO_2 by PC60-NaX increases, and the separation ratio of CO_2/H_2O is also improved. In the experiment, the increase in the adsorption capacity of PC60-NaX for low concentration (400 ppm) CO_2 resulted in a longer breakthrough time, as shown in Figure 7d. The breakthrough curve of PC60-NaX for CO_2 adsorption is steeper. This indicates that compared to the original zeolite, the adsorption of CO_2 by PC60-NaX has almost no mass transfer limitations. The slope of the penetration curve of PC60-NaX for H_2O adsorption becomes slower, showing a restriction on the mass transfer of H_2O. The adsorption penetration time reflects the adsorption efficiency and adsorption selectivity of the adsorbent. The longer the adsorption penetration time, the higher the adsorption efficiency and the stronger the adsorption selectivity of the adsorbent. (Figure 7d; and Tables S9 and S10, Supporting Information).

Due to the competitive adsorption relationship between CO_2 and H_2O, the mass transfer rate and adsorption selectivity of H_2O are better than that of CO_2. Therefore, as CO_2 and H_2O are co-adsorbed, the released adsorption heat will cause CO_2 to be desorbed preferentially. The lag in adsorption breakthrough time proves that the pore structure or morphology of PC60-NaX changes, causing CO_2 to be "locked". From a thermodynamic perspective, it is believed that there are differences in the interaction strengths between CO_2 and H_2O molecules and the PC60-NaX surface. From a kinetic perspective, it is believed that the adsorption bed in which CO_2 and H_2O compete for adsorption is always in a non-isothermal state. As the bed temperature has a gradient distribution of heating or cooling, the thermal motion properties of molecules and the adsorption/desorption capabilities of different positions in the bed change. The energy consumption during the desorption process of the saturated NaX zeolite is assessed by differential thermal analysis (DSC). Compared with the original zeolite, PC60-NaX consumes more heat in the desorption process, as shown by the increase from 6.31 to 6.68 kJ mol g^{-1} (Figure S12, Supporting Information). The breakthrough curves of PC60-NaX at relative humidity (20/40/80%) within the study range are all very steep, demonstrating its excellent gas diffusion capacity (Figure S13, Supporting Information). However, it is difficult to inhibit the competitive adsorption of CO_2 and H_2O by physical adsorption through non-chemical means, so the adsorption of CO_2 by PC60-NaX is still limited in a high humidity environment. However, the competitive adsorption of CO_2 and H_2O by physical adsorbents can be effectively controlled through surface modification, control of operating conditions, dynamic adsorption and desorption cycles, and multilayer adsorbent system design,[44,46] thereby enhancing the adsorption efficiency of CO_2.

The kinetic sieving effect is a method to achieve separation based on the differences in the diffusion rates of different gas molecules in the molecular sieve channels. When gas adsorption cannot reach equilibrium, kinetic separation may occur. The gas diffusion rate is determined from its diffusion constant, which can be obtained by fitting the time-dependent gas absorption curve of a given adsorbent to known solutions of the diffusion equation in different crystalline adsorbent forms. By comparing the diffusion coefficients of different gases in the selected adsorbent and the time required to reach adsorption equilibrium under certain conditions, the possibility of kinetic separation of a certain gas mixture by the adsorbent can be predicted. PC60-NaX molecular sieve has enhanced CO_2 adsorption capacity due to its pore confinement and multiple cation effects, as shown in Figure 7d. Therefore, based on the kinetic differences in the adsorption of CO_2 and H_2O exhibited by PC60-NaX, efficient kinetic screening of CO_2/H_2O is achieved.

The cycling stability of PC60-NaX is evaluated by conducting 5 consecutive adsorption/desorption operations at 180 °C for 1 h each time. As shown in Figure 7e, PC60-NaX treated with in situ plasma CO_2 has good stability with the adsorption capacity maintained at ≈5.47 mmol g^{-1}. After 5 consecutive adsorption/desorption operations, the adsorption capacity only decreases by 0.27% ((q_{sta}-q_{end}) / q_{sta}). To further explore the hydrothermal stability of PC60-NaX, it is treated with water vapor at 180 °C for 20 h. Figure 7f shows that the adsorption performance only changes by 0.49%. By considering the possible influence of the ambient airflow, the change in the PC60-Na adsorption mass is acceptable.

Table S1 (Supporting Information) shows that the NaX zeolite samples after long-term (180 min) CO_2 and N_2 (60 min) treatments have larger specific surface areas. However, the adsorption selectivity for CO_2 is not high. This is because CO_2^* causes O-T-O (T = Al, Si) to transform into the carbonate form as the treatment time increases. The transformation destroys a part of the porous structure in the NaX zeolite and increases the surface area. However, owing to the formation of carbonate, the adsorption sites of CO_2 are occupied, and therefore, the adsorption capacity decreases.

N_2, a non-polar molecule, diffuses into the NaX porous structure at high pressure instead of adsorbing onto the surface. The plasma forms $N_2^{+,}$ and under the influence of the E-field, some ion bombardment and etching effects are produced[47] to change the surface area of the NaX zeolite. They also change the surface electrostatic potential energy of O-T-O (T = Al, Si) and reduce the adsorption selectivity for the polar CO_2 molecule.

In addition, the common 3A and 5A zeolites are studied. In larger commercial zeolites, in situ plasma CO_2 treatment can also

improve the adsorption performance of zeolites for low concentrations of CO_2. Among them, the NaX zeolite shows the most obvious improvement. This may be related to the twelve-binary ring skeleton of the NaX zeolite. The larger skeleton frame allows more changes in the structure of the zeolite. In general, the in situ plasma CO_2 treatment improves the affinity of zeolite to CO_2. This not only is reflected by the changes in adsorption capacity and adsorption energy, but also makes zeolite have higher trapping efficiency at a low concentration of CO_2.

3. Conclusion

The carbon dioxide capture properties of the modified NaX zeolite are determined. Owing to the E-field formed by the plasma and exposure to CO_2, it morphs into a stable low-energy structure that can accommodate more CO_2. By increasing the surface area and adsorption sites for CO_2, the NaX zeolite, after the dual plasma treatment and CO_2 exposure for 60 min, shows the highest adsorption capacity of 5.49 mmol g^{-1}. By increasing the desorption energy consumption of the NaX zeolite by 5.88%, more efficient and larger-capacity low-concentration carbon dioxide capture can be accomplished. In addition, in the environment with a relative humidity of 40%, the separation ratio of PC60-NaX for CO_2 and H_2O is 0.107 mol mol^{-1}, consequently greatly enhancing the application potential of the materials in humid environments. The cycling stability and hydrothermal stability of PC60-NaX are also demonstrated to be excellent. The competitive adsorption mechanism of CO_2 and H_2O on PC60-NaX is comprehensively analyzed from the perspectives of adsorption equilibrium and adsorption kinetics, and verified by thermodynamics and kinetics. This principle can guide the design and optimization of adsorption processes, as well as the regeneration and replacement of adsorbents. These findings reveal the changes in zeolite structure produced by cold plasma-induced electric fields and active species. This result broadens the application prospects of porous structure control based on surface modification, modification, and doping of cold plasma materials, especially the multi-objective optimization of porous structures at low temperatures. Combined with the application scenarios of cold plasma, this strategy also promotes the development and application of new materials, such as nanomaterials, biocompatible materials, etc. These new materials show great application potential in the fields of energy, environmental protection, biomedicine and other fields.

4. Experimental Section

Materials: The commercial NaX zeolite samples were purchased from China Luoyang Jianlong Micro-Nano New Materials Co., Ltd. The cold plasma treatment was conducted with the bipolar DBD using an input voltage of 220 V and an output electric field of 200 kV m^{-1}. This device currently uses a certified capacitance and voltage device. According to the calculation formula of the electric field in the dielectric barrier discharge system:

$$E = \frac{V}{d}\left(\frac{\in_r + 1}{2}\right) \tag{2}$$

where $\in_r$ is the relative permittivity of the dielectric material. The total electrode spacing is d and the applied voltage is V. The total electrode spacing d includes the thickness of the dielectric layer and the gas layer. The applied voltage V is 220 volts, the total electrode spacing d is 2.75 nm, and the relative dielectric constant $\in_r$ is 4.

One gram of commercial NaX zeolite was placed between DBD and 1 atm (CO_2/N_2/Ar atmosphere) for 10 min to generate an in situ environment. Under different in situ environment treatments, the samples were named PC30-NaX, PC60-NaX, PC90-NaX, PC120-NaX, PC180-NaX, PN60-NaX (N_2), and PA60-NaX (Ar) according to the treatment time.

Characterization and Instruments: Scanning electron microscopy (SEM) was performed to examine the morphology and crystal surface and the elemental information was acquired by energy-dispersive X-ray spectroscopy (EDS) on the NOVA NANOSEM 230 and EDS X-MAX50 (FEI, USA). XRD was conducted to analyze the crystal structures on the Bruker D8 Advance (Germany) Cu K_α irradiation (1.5405 nm) in the range of 5–50° using steps of 0.04°, time of 2 s for each step, current of 10 mA, and voltage of 40 kV.

The porous structure was examined on the physical adsorption instrument (Micrometric, USA). The sample was degassed at a temperature of 100 °C in vacuum for 12 h and then N_2 physical adsorption was carried out at −196 °C to determine the specific surface, pore volume, pore size, and other parameters. The adsorption isotherm and adsorption/desorption curves of CO_2 were acquired in a high-purity CO_2 environment at 0 °C.

X-ray photoelectron spectroscopy (XPS) was carried out on the Thermo SCIENTIFIC ESCALAB 250Xi using monochromatic Al K_α X-ray with an energy of 1486.68 eV. The spectra were referenced to the C*1s* peak at 285.0 e V, and the quantitative analysis was conducted after removing the nonlinear (Shirley) background. In situ FTIR was performed on the Bruker Vertex 80 spectrometer (Germany) to determine the adsorption characteristics of CO_2. Before the test, the sample was dried at 100 °C in nitrogen for 12 h. The desorbed sample was placed in a 5 ml reactor and cooled to 40 °C before 99.999% CO_2 was introduced to study the adsorption phenomenon for 10, 20, 30, 40, 50, and 60 min. In situ Raman spectroscopy was tested by Horiba scientific-LabRAM HR evolution (Japan). The sample was processed by in situ infrared and the test time was increased to 90 min.

Gas Adsorption/Desorption Experiment: The temperature-programmed adsorption/desorption properties were determined by thermogravimetric analysis using the Setline equipment (France). The sample was heated from room temperature (25 °C) to 180 °C under flowing nitrogen (40 mL min^{-1}) at a ramping rate of 10 °C min^{-1} prior to cooling to 40 °C after 60 min to achieve complete desorption. The adsorption capacity of CO_2 was determined at a flow rate of 40 mL min^{-1} of 400 ppmCO_2/N_2 by switching the air streams. The adsorption capacity of the sample for CO_2+H_2O was determined at 400 ppm CO_2/N_2 + water vapor (20/40/80% RH by adjusting the temperature of the water bath) at a flow rate of 40 mL min^{-1}. The desorption characteristics including the concentration changes of CO_2 and H_2O were studied on the flue gas analyzer (Shenzhen Watersey Co., Ltd.).

The multi-component competitive adsorption test uses an adsorption analyzer model BSD-MAB to detect the import and export gases by online mass spectrometry. The sample was first purged by N_2 heating at 200 °C for 2 h for complete desorption regeneration. The sample was then weighed and loaded into a penetration column with an inner diameter of 6 mm, and the loading length was 47 mm. Simulated air (101.5 kPa) was fed, consisting of 400 ppm CO_2 and water vapor with 40% relative humidity and N_2 as carrier gas.

DFT Calculation: The calculation uses a periodic model and uses the VASP program package for structural optimization, and the Na^+ site located near O-T-O (T = Al, Si) was selected as the CO_2 adsorption site in the theoretical calculation. This site had been widely recognized as the active site of NaX molecular sieve reaction. The electron-ion Coulomb interaction in the calculation process was described using the all-electron projection plus wave (the projector augmented wave.PAW). The exchange correlation effect uses the generalized gradient approximation (thegeneralized gradient approximation. GGA) and the Perdew-Burke-Ernzerhof (PBE) functional. The semi-empirical DFT-D3 was used to describe the van der Waals interaction between molecular sieve channels and adsorbed species. The cutoff energy of the plane wave basis set was set to 500 eV, the Brillouin zone sampling uses the gamma point, the unit cell size was

$1 \times 1 \times 1$, the energy convergence standard was 10^{-5} eV uc^{-1}, and the force convergence standard was 0.03 eV $Å^{-1}$. The unadsorbed structure was optimized using full relaxation to obtain the lowest energy and most stable initial structure, and then in the structure containing the adsorbed species. In order to reduce calculation time, all atoms in the active site center structure and adsorbed molecules were optimized by full relaxation, and the remaining molecular sieve skeleton atoms remain fixed. All image processing was done on VESTA.[48]

NaX consists of six rings connected by oxygen bridges to form a hexagonal column cage with the β cage surrounding the main crystal cavity of X zeolite (a large and eight-sided zeolite cage). The eight-sided zeolite cage is connected through twelve rings (X-type zeolite main crystal pores) to form a cell. Considering the influence of the skeleton and pores on the adsorption process, some supercage structures were selected to simplify the calculation process. The clusters were enclosed by hydrogen, and the O atoms at the edges were replaced by H atoms.[49] In the process of geometric optimization, the space geometric coordinates of substituted H atoms were fixed to ensure that the clusters had the characteristics of X-type zeolite. The rest of the atoms, including the metal ion in the center of the hole, were in the relaxed state. In this way, the structure of the active metal and twelve binary rings could be adjusted during geometric optimization to produce the most stable structure.

Since it was difficult to check the electric field intensity directly using the Materials studio software, the codes were entered manually when adding the electric field intensity. The input file in the dialog box of the Dmol3 module was created with the keyword of "electric-field x y z" representing the electric field components in the x, y, and z directions, respectively. The unit of the electric field in the software was Hartree/Bohr (1 Hartree/Bohr = 52 V $Å^{-1}$). The electric field strength of the DBD equipment was 200 kV m^{-1} and after conversion, the output form was "electric-field 0.000 0.000 0.0004".[21]

Supporting Information

Supporting Information is available from the Wiley Online Library or from the author.

Acknowledgements

This work was supported by the National Key Research and Development Program of China (No. 2022YFC3800401), China Scholarship Council (Grant No. 202306460067), Beijing Natural Science Foundation (Grant No. 3232043), and City University of Hong Kong Donation Research Grants (DON-RMG 9229021 and 9220061). The authors would like to express the sincere gratitude to Pro Lu Qipeng for generously providing the software and granting the necessary permissions for its usage in this research. The availability of Materials Studio significantly contributed to the success of the experiments conducted in this study.

Conflict of Interest

The authors declare no conflict of interest.

Data Availability Statement

The data that support the findings of this study are available from the corresponding author upon reasonable request.

Keywords

CO_2, cold plasma, direct air carbon capture, physical adsorption

Received: May 23, 2024
Revised: July 9, 2024
Published online: August 7, 2024

[1] M. Shen, F. Kong, L. Tong, Y. Luo, S. Yin, C. Liu, P. Zhang, L. Wang, P. K. Chu, Y. Ding, *Carbon Neutrality* **2022**, *1*, 37.
[2] A. Gambhir, M. Tavoni, *One Earth* **2019**, *1*, 405.
[3] H. Li, M. E. Zick, T. Trisukhon, M. Signorile, X. Liu, H. Eastmond, S. Sharma, T. L. Spreng, J. Taylor, J. W. Gittins, *Nature* **2024**, *630*, 654.
[4] M. Shen, Z. Hu, F. Kong, L. Tong, S. Yin, C. Liu, P. Zhang, L. Wang, Y. Ding, *Rev. Environ. Sci. Bio/Technol.* **2023**, *22*, 823.
[5] J. Sun, M. Zhao, L. Huang, T. Zhang, Q. Wang, *Curr. Opin. Green Sustainable Chem.* **2023**, *40*, 100752.
[6] T. Terlouw, K. Treyer, C. Bauer, M. Mazzotti, *Environ. Sci. Technol.* **2021**, *55*, 11397.
[7] M. Erans, E. S. Sanz-Pérez, D. P. Hanak, Z. Clulow, D. M. Reiner, G. A. Mutch, *Energy Environ. Sci.* **2022**, *15*, 1360.
[8] L. Küng, S. Aeschlimann, C. Charalambous, F. McIlwaine, J. P. Young, N. Shannon, K. Strassel, C. N. Maesano, K. Kahsar, D. Pike, *Energy Environ. Sci.* **2023**, *16*, 4280.
[9] S. Chowdhury, Y. Kumar, S. Shrivastava, S. K. Patel, J. S. Sangwai, *Energy Fuels* **2023**, *37*, 10733.
[10] X. Zhu, W. Xie, J. Wu, Y. Miao, C. Xiang, C. Chen, B. Ge, Z. Gan, F. Yang, M. Zhang, *Chem. Soc. Rev.* **2022**, *51*, 6574.
[11] D. Fu, M. E. Davis, *Chem. Soc. Rev.* **2022**, *51*, 9340.
[12] M. Song, G. Rim, F. Kong, P. Priyadarshini, C. Rosu, R. P. Lively, C. W. Jones, *Ind. Eng. Chem. Res.* **2022**, *61*, 13624.
[13] R. Zhao, L. Liu, L. Zhao, S. Deng, S. Li, Y. Zhang, *Renewable Sustainable Energy Rev.* **2019**, *114*, 109285.
[14] D. Fu, Y. Park, M. E. Davis, *Proc. Natl. Acad. Sci. USA* **2022**, *119*, 2211544119.
[15] L. Liu, S. Jin, K. Ko, H. Kim, I.-S. Ahn, C.-H. Lee, *Chem. Eng. J.* **2020**, *382*, 122834.
[16] J. M. Findley, D. S. Sholl, *J. Phys. Chem. C.* **2021**, *125*, 24630.
[17] D. Fu, Y. Park, M. E. Davis, *Angew. Chem., Int. Ed.* **2022**, *61*, 202112916.
[18] S. K. Wahono, A. A. Dwiatmoko, A. Cavallaro, S. C. Indirathankam, J. Addai-Mensah, W. Skinner, A. Vinu, K. Vasilev, *Plasma Processes Polym.* **2021**, *18*, 2100028.
[19] M. R. Cesario, D. A. de Macedo, *Heterogeneous Catalysis: Materials and Applications*, Elsevier, Amsterdam **2022**.
[20] A. Jafarzadeh, K. M. Bal, A. Bogaerts, E. C. Neyts, *J. Phys. Chem. C.* **2020**, *124*, 6747.
[21] K. Chen, Z. Yu, S. H. Mousavi, R. Singh, Q. Gu, R. Q. Snurr, P. A. Webley, G. K. Li, *Nat. Commun.* **2023**, *14*, 5479.
[22] X. Li, H. Li, G. Yang, *J. Colloid Interface Sci.* **2017**, *501*, 54.
[23] H. Xiong, D. Devegowda, L. Huang, *Langmuir* **2020**, *36*, 723.
[24] M. Si, D. Wang, R. Zhao, D. Pan, C. Zhang, C. Yu, X. Lu, H. Zhao, Y. Bai, *Adv. Sci.* **2020**, *7*, 1902538.
[25] X. Yue, J. Fan, Q. Xiang, *Adv. Funct. Mater.* **2022**, *32*, 2110258.
[26] T. Meng, B. Li, Q. Wang, J. Hao, B. Huang, F. L. Gu, H. Xu, P. Liu, Y. Tong, *ACS Nano* **2020**, *14*, 7066.
[27] M. Ding, X. Liu, P. Ma, J. Yao, *Coord. Chem. Rev.* **2022**, *465*, 214576.
[28] Y. Guo, J. Sun, R. Wang, W. Li, C. Zhao, C. Li, J. Zhang, *Carbon Capture Sci. Technol.* **2021**, *1*, 100011.
[29] M. M. Zagho, M. K. Hassan, M. Khraisheh, M. A. A. Al-Maadeed, S. Nazarenko, *Chem. Eng. J. Adv.* **2021**, *6*, 100091.
[30] X. Zhu, Y. Sun, Y. Liu, X. Sun, J. Shi, *Sep. Sci. Technol.* **2022**, *57*, 2885.
[31] P. Bhatt, R. Singh, N. Yadav, R. Shanker, *Phys. Rev. A.* **2010**, *82*, 044702.
[32] Y. Wang, B. Liu, X. a. Zhao, X. Zhang, Y. Miao, N. Yang, B. Yang, L. Zhang, W. Kuang, J. Li, *Nat. Commun.* **2018**, *9*, 4058.
[33] M. Santoro, F. Gorelli, J. Haines, O. Cambon, C. Levelut, G. Garbarino, *Proc. Natl. Acad. Sci. USA* **2011**, *108*, 7689.
[34] X. Sun, J. Bao, K. Li, M. D. Argyle, G. Tan, H. Adidharma, K. Zhang, M. Fan, P. Ning, *Adv. Funct. Mater.* **2021**, *31*, 2006287.

[35] L. Deng, H. Hu, Y. Wang, C. Wu, H. He, J. Li, X. Luo, F. Zhang, D. Guo, *Appl. Surf. Sci.* **2022**, *604*, 154459.
[36] M. Kaseem, S. Fatimah, N. Nashrah, Y. G. Ko, *Prog. Mater Sci.* **2021**, *117*, 100735.
[37] Z. Zhang, W. Zhang, X. Chen, Q. Xia, Z. Li, *Sep. Sci. Technol.* **2010**, *45*, 710.
[38] J. McEwen, J.-D. Hayman, A. O. Yazaydin, *Chem. Phys.* **2013**, *412*, 72.
[39] J. Guo, H. Wu, Y. Wei, Y. Miao, J. Qu, P. Wang, *RSC Adv.* **2024**, *14*, 1686.
[40] K. L. T. Nguena, C. G. Fotsop, S. B. L. Ngomade, A. K. Tamo, C. A. Madu, F. Ezema, E. E. Oguzie, *Mater. Today Commun.* **2023**, *37*, 107406.
[41] A. Ramirez, X. Gong, M. Caglayan, S.-A. F. Nastase, E. Abou-Hamad, L. Gevers, L. Cavallo, A. Dutta Chowdhury, J. Gascon, *Nat. Commun.* **2021**, *12*, 5914.
[42] S. Starikovskaia, K. Allegraud, O. Guaitella, A. Rousseau, *J. Phys. D: Appl. Phys.* **2010**, *43*, 124007.
[43] S. U. Rege, R. T. Yang, *Chem. Eng. Sci.* **2001**, *56*, 3781.
[44] M. Shen, F. Kong, W. Guo, Z. Zuo, T. Gao, S. Chen, L. Tong, P. Zhang, L. Wang, P. K. Chu, *Chem. Eng. J.* **2024**, *479*, 147923.
[45] V. R. Mollo-Varillas, F. Bougie, M. C. Iliuta, *Sep. Purif. Technol.* **2022**, *282*, 120008.
[46] Y. Yang, Y. Chen, Z. Xu, L. Wang, P. Zhang, *Sep. Purif. Technol.* **2020**, *237*, 116335.
[47] K. H. Rouwenhorst, H.-H. Kim, L. Lefferts, *ACS Sustainable Chem. Eng.* **2019**, *7*, 17515.
[48] X. Chen, B.-X. Shen, H. Sun, G.-X. Zhan, *Ind. Eng. Chem. Res.* **2017**, *56*, 10164.
[49] X. Chen, B. Shen, H. Sun, *Microporous Mesoporous Mater.* **2018**, *261*, 227.

Supporting Information

Enhanced Direct Air Carbon Capture on NaX Zeolite by Electric-Field Enhanced Physical Adsorption and *In Situ* CO_2 Synergistic Effects of Cold Plasma

Minghai Shen1,2,4, Fulin Kong1,2, Wei Guo1,2, Zhongqi Zuo1,2, Chan Guo3, Lige Tong1,2*, Shaowu Yin1,2, Li Wang1,2, Sibudjing Kawi4*, Paul K. Chu5*, Yulong Ding6*

Table of Contents

Adsorption isotherm model

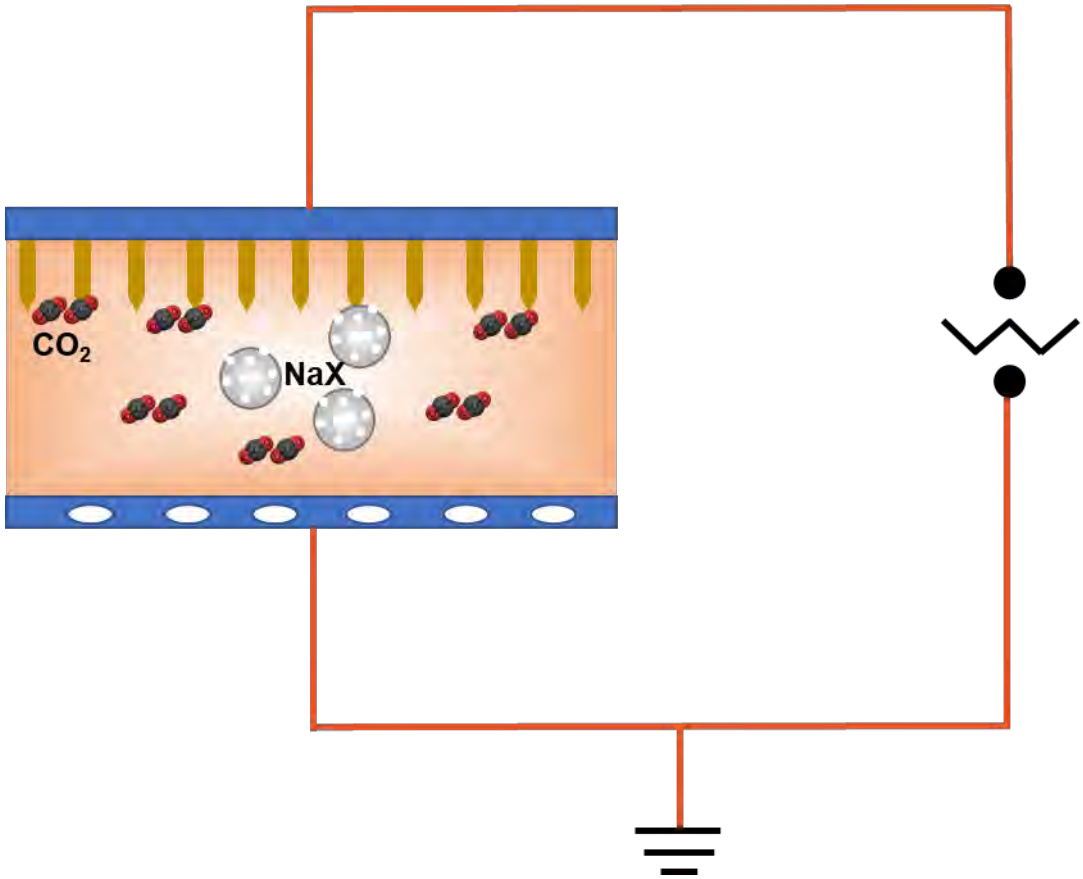

Figure S1. Schematic diagram of the *in situ* CO_2 treatment of the NaX zeolite by DBD.

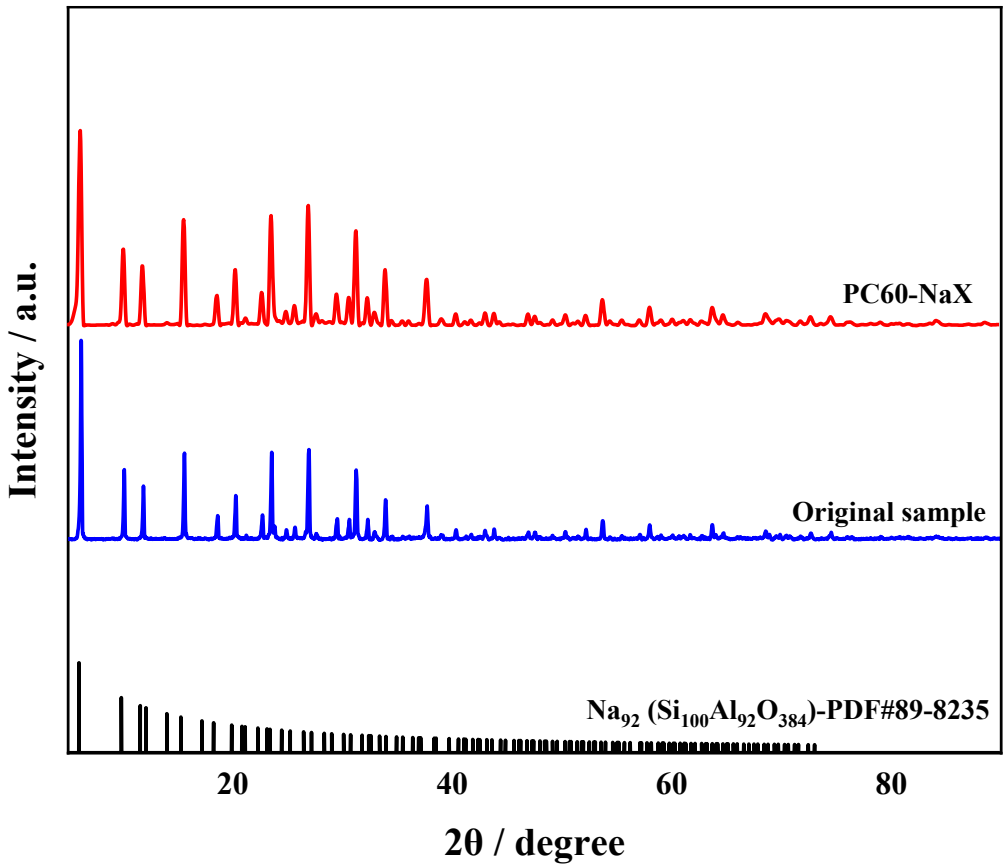

Figure S2. XRD patterns of the modified NaX zeolite by the *in situ* CO_2 plasma treatment.

Table S1. Specific surface and pore size parameters of the NaX zeolite after treatment in different atmospheres.

Parameters		Original sample	Plasma CO_2-60min	Plasma CO_2-180min	Plasma N_2-60min
Specific surface area	Single point method for specific surface area（m^2/g）	593.0174	628.6347	731.9611	672.6461
	BET Surface Area（m^2/g）	596.2447	629.6685	733.4421	675.0227
Pore volume	Single point method pore capacity（cm^3/g）	0.325997	0.319672	0.385597	0.348814
Pore size	Adsorption average pore diameter (4V/A by BET)（nm）	2.1870	2.0307	2.1029	2.0670
	BJH Adsorption average pore width (4V/A) nm）	8.9558	9.3813	15.8586	10.8173

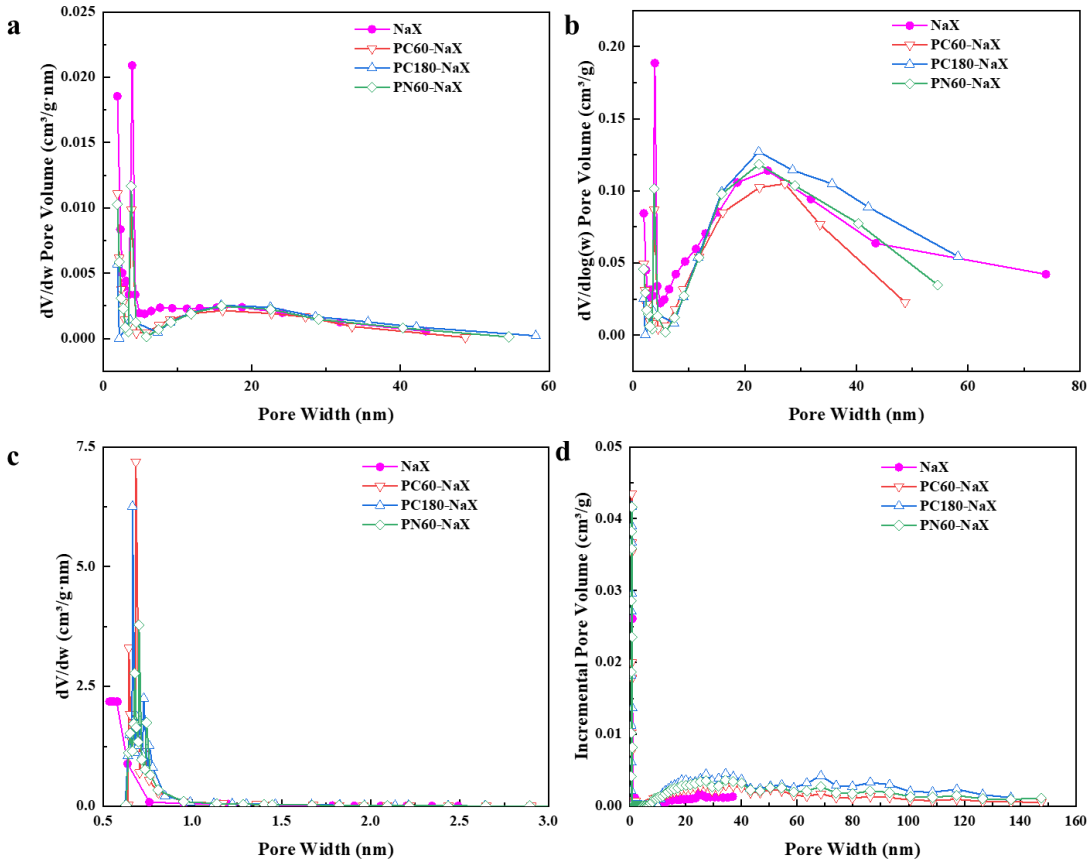

Figure S3. Pore parameters of the NaX zeolite treated with CO_2 and N_2 plasmas: (a) Pore distributions for adsorption and desorption by the BJH method and logarithmic distributions; (b, c) HK aperture distributions; (d) Cumulative pore volumes.

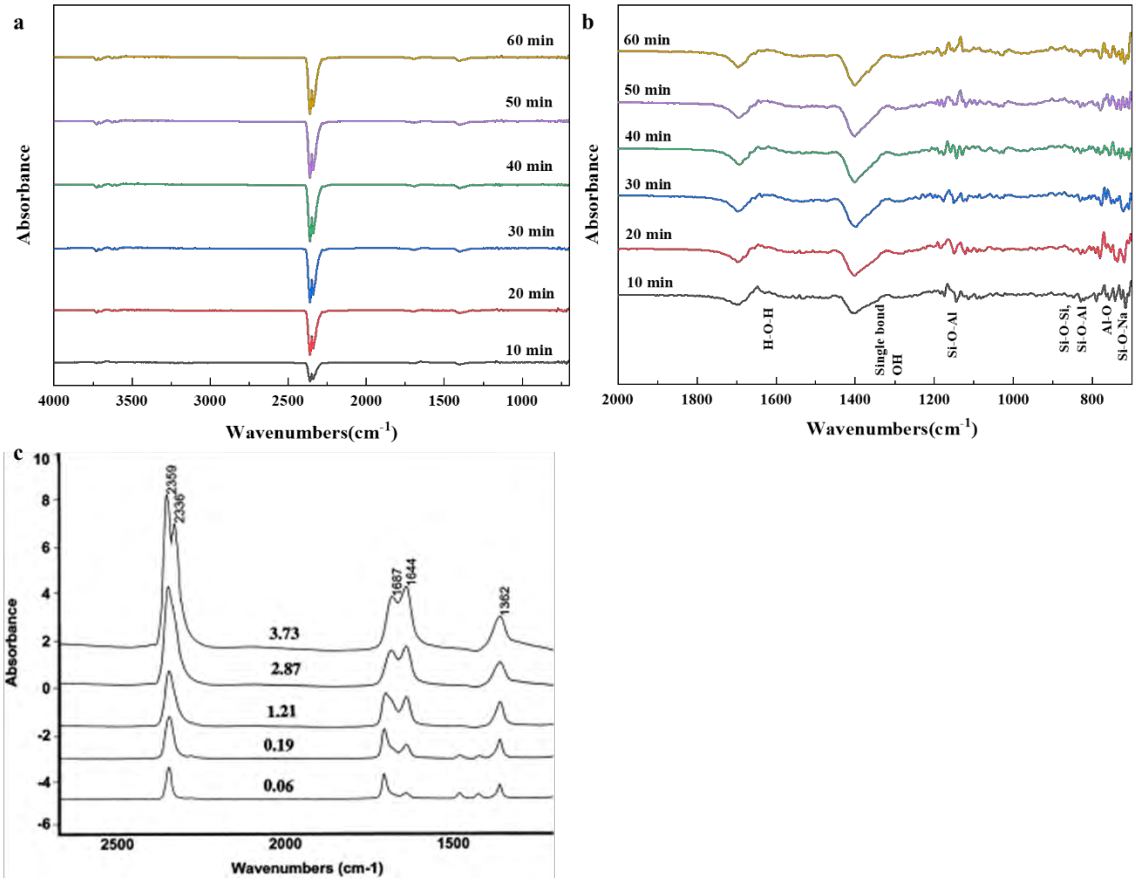

Figure S4. Infrared absorption spectra of PC60-NaX in the *in situ* CO_2 environment: (a) Overall spectra and (b) Peaks in the 700 cm^{-1} – 2000 cm^{-1} range of the NaX zeolite; (c) Infrared spectra of pure component CO_2 at different concentration ratios (0.1-4% v=v) at 295 K on NaX zeolite in the literature. [1]

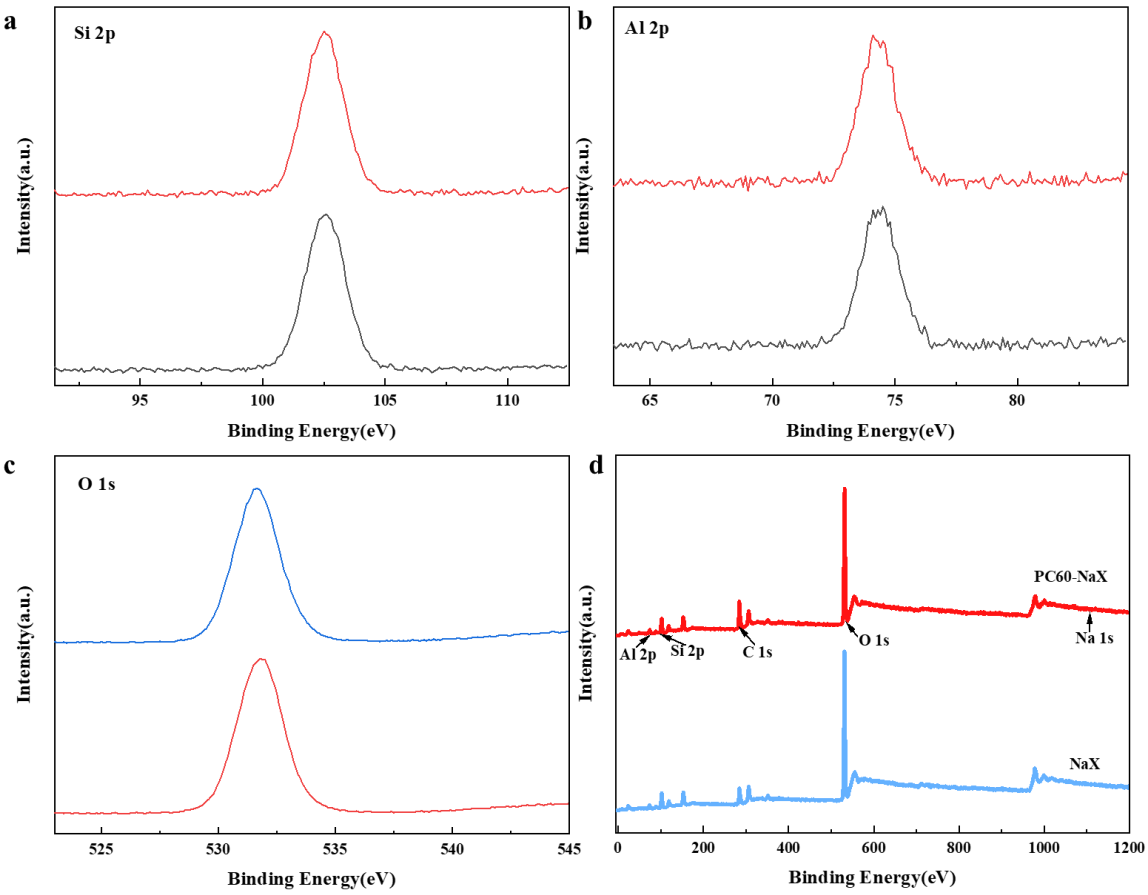

Figure S5. XPS spectra of PC60-NaX: (a) Si *2p*, (b) Al *2p*, (c) O *1s*, (d)full spectra.

Table S2. Effects of CO_2 and applied electric field on O-T-O (T = Al, Si) bond length and bond angle.

Parameters		Original structure	CO_2 addition optimization	Original structure + applied electric field	Add CO_2 + applied electric field
Structure diagram		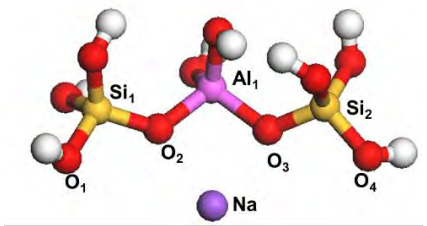	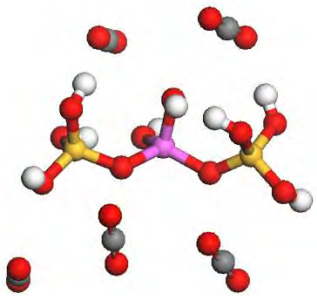	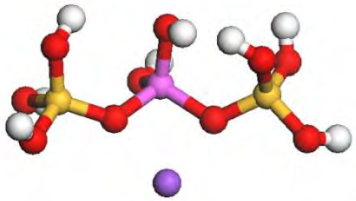	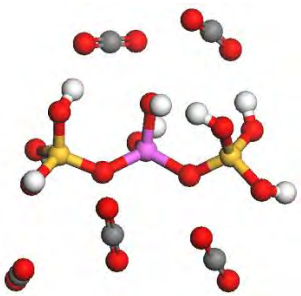
Bond length	O_1-Si_1	1.662	1.716	1.663	1.716
	Si_1-O_2	1.653	1.729	1.653	1.731
	O_2-Al_1	1.802	1.880	1.801	1.882
	Al_1-O_3	1.807	1.868	1.806	1.867
	O_3-Si_2	1.657	1.732	1.657	1.729

	Si_2-O_4	1.663	1.717	1.663	1.718
Distance	Na- Al_1	3.228	4.278	3.227	4.510
Bond Angle	O_1-Si_1-O_2	108.115	111.894	108.649	110.044
	O_2-Al_1-O_3	100.739	130.683	100.892	134.281
	O_3-Si_2-O_4	109.263	109.652	108.931	109.808

Table S3. Adsorption of CO_2 at the top sites on O-T-O (T = Al, Si).

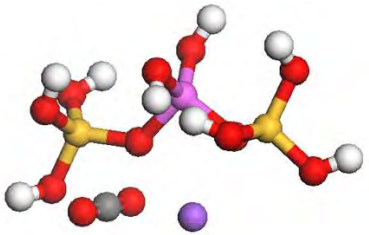
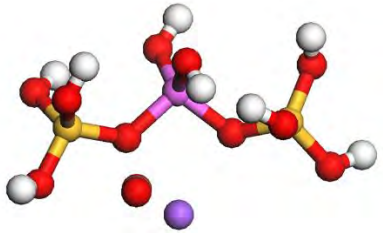
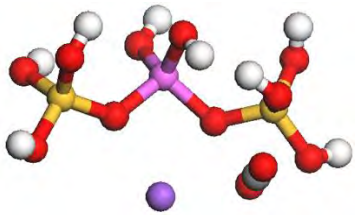
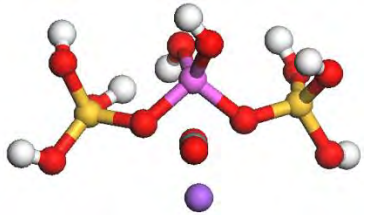

	CO_2 adsorption on Si_1		CO_2 adsorption on Al_1		CO_2 adsorption on Si_2		CO_2 adsorption on the O_1 between Si_1 and Al_1	
	Original	After electric field treatment	Original	After electric field treatment	Original	After electric field treatment	Original	After electric field treatment
Distance	4.336	3.868	2.157	2.203	2.052	4.115	3.568	3.702
Adsorption energy (kcal/mol)	-2.364	-2.028	-7.596	-6.396	-5.600	-1.733	-2.142	-2.508

Adsorption isotherm model

The adsorption isotherm models are based on different assumptions, and there is no specific isotherm model that is universally applicable to all experimental data. [2] In addition, in some cases, the assumptions of the model cannot describe the experimental data and the situation absolutely requires the use of multiple isotherm models for adsorption data analysis. The Langmuir isotherm assumes that monolayer adsorption has a certain number of adsorption sites on a uniform surface. In contrast, the Freundlich model is more suitable for heterogeneous surfaces that can be applied to multilayer adsorption. These two models are the most popular when describing the properties of adsorbents. The Tempkin isotherm assumes that the decrease in adsorption heat is linear. The Dubinin-Radushkevich isotherm is commonly used to determine whether the adsorption mechanism is chemical or physical, heterogeneous surfaces with free energy on the surface.

Langmuir isotherm model

The Langmuir isotherm model is based on the assumption that the surface of the adsorbent is uniformly distributed and that all adsorption sites have the same probability of adsorbing molecules. In the adsorption process, the adsorbent is adsorbed in a single layer on the surface of the adsorbed material. When the adsorption equilibrium is reached, the adsorption rate and desorption rate are the same. The expression is shown in *Eq*. (1): [3]

$$q = Aq_e \frac{\frac{p}{p_0}}{1+A\frac{p}{p_0}}, \quad (1)$$

Where p(Pa) is the pressure, p_0 (Pa) is the saturated vapor pressure, q is the adsorption amount at adsorption equilibrium (mmol·g^{-1}), A is Langmuir correlation constant, and q_e is the maximum adsorption capacity (mmol·g^{-1}).

Freundlich isotherm model

The Frundlich isotherm, another adsorption isotherm, is a special example of an inhomogeneous surface energy, which is basically an empirical formula and generally used for low concentrations. The expression is: [4]

$$q = B(\frac{p}{p_0})^{\frac{1}{n}}, \tag{2}$$

where q is the adsorption capacity, $\frac{p}{p_0}$ is the adsorption mass equilibrium pressure, and B and n are constants. Under normal circumstances, the above formula is rewritten into the logarithmic one, $\frac{p}{p_0}$ and the corresponding q point are drawn on the double logarithmic coordinate paper to obtain an approximate straight line.

Temkin Isotherm model

The Temkin model is a kind of real models meaning that the adsorption heat of adsorbent on the surface decreases linearly with the increase in the covering degree. Temkin postulates that the adsorption enthalpy changes linearly with the partial pressure of the gas. [5] The Temkin isotherm considers the indirect interaction between adsorbent molecules and assumes that it is due to the adsorbent-adsorbent interaction. The adsorption heat of all molecules in the layer decreases linearly with coverage, and the adsorption is characterized by a uniform distribution of the binding energy and the maximum binding energy. The Temkin isotherm model has been used in the linear form as shown by formula (3): [6]

$$q = b \ln a + b \ln \frac{p}{p_0}, \tag{3}$$

Where $b = RT \cdot c^{-1}$. c is the Temkin constant related to adsorption heat ($J \cdot mol^{-1}$), a is the Temkin isotherm constant ($L \cdot g^{-1}$), R is the universal gas constant (8.314) $J \cdot mol^{-1}$, and T is the absolute temperature (K).

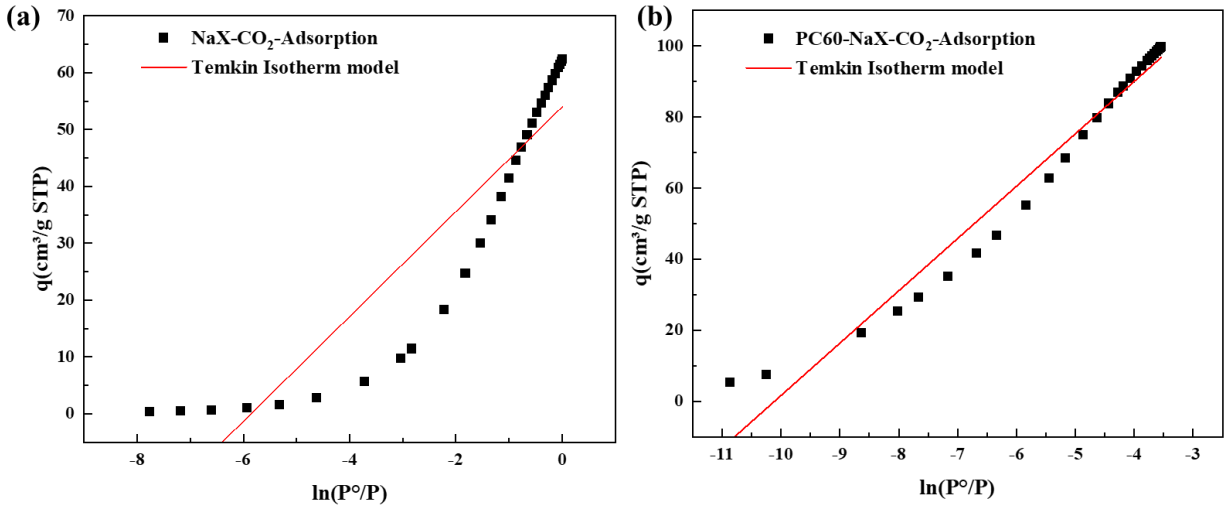

Figure S6. Temkin isothermal model for CO_2 adsorption: (a) NaX and (b) PC60-NaX.

Dubinin-Radushkevich Isotherm model

Compared to surface adsorption, the adsorption potential of microporous filling is stronger, and micropores can capture adsorbent molecules at very low relative pressure. Based on the theory of adsorption and adhesion potential, the effects of the pore size distribution of zeolite on adsorption and the interaction of the working forces between the particles are considered. The adsorbent is stored in the micropores by filling rather than the surface covering described by L-type and BET type, which more truly reflects the adsorption mechanism of adsorbed gas in the micropore. The Dubinin-Radushkevich model (simply called "D-R model") is for the adsorbent micropore, and the adsorption equation for the gas can be expressed by equation (1): [7]

$$\ln q = q_e + K \ln\left(\frac{p}{p_0}\right)^2 , \qquad (4)$$

Where q is the absorption capacity at pressure p in mmol·g^{-1}, q_e is the saturation and adsorption capacity in mmol·g^{-1}, and K is the comprehensive constant that is related to the net heat of absorption.

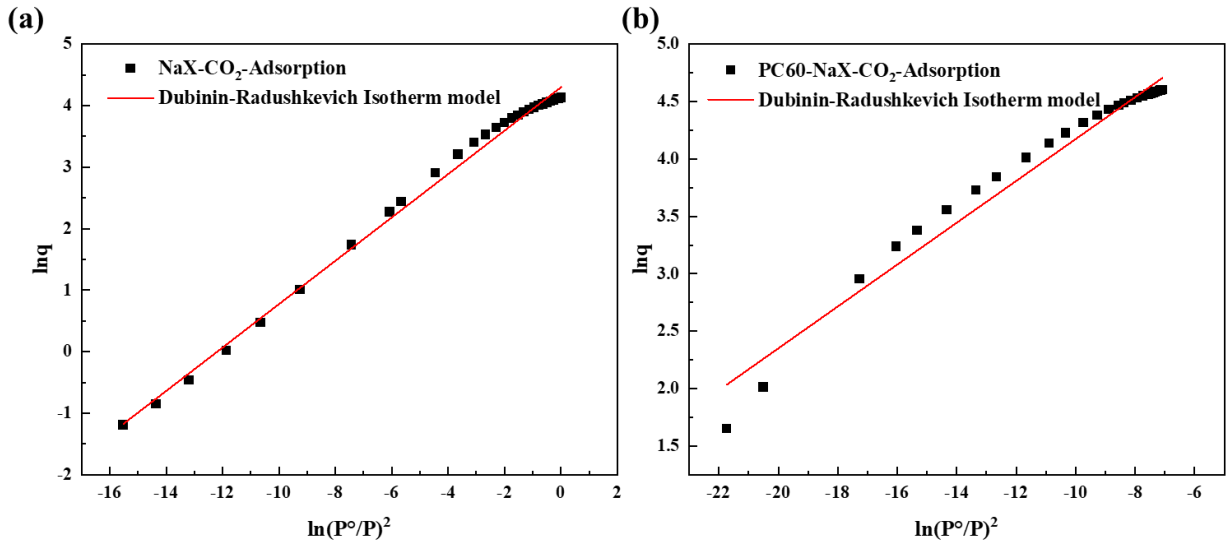

Figure S7. D-R model for CO_2 adsorption: (a) NaX and (b) PC60-NaX.

Table S4 Parameters of CO_2 adsorption isotherm of NaX and PC60-NaX with different models.

Isotherm model	Parameters	NaX	PC60-NaX
Langmuir isotherm model	q_e	81.46	103.14
	A	2.46	483.99
	R^2	0.99	0.97
Freundlich isotherm model	B	65.18	285.76
	n	2.00	3.47
	R^2	0.98	0.98
Temkin Isotherm model	a	349.85	24621.62
	b	9.21	14.73
	R^2	0.85	0.96
D-R model	q_e	4.30	6.00
	K	0.35	0.18
	R^2	0.99	0.97

Kinetics study

The adsorption data of NaX and PC60-NaX are fitted by pseudo-first-order kinetic equation and pseudo-second-order kinetic equation. To explore the adsorption kinetics of PC60-NaX modified by modified plasma and CO_2. The pseudo-first-order (PFO) kinetic equation is as follows:

$$q = q_e(1 - e^{-k_1 t}) \ . \tag{5}$$

The pseudo-second-order (PSO) kinetic equation is as follows:

$$\frac{t}{q_t} = \frac{1}{k_2 q_e^2} + \frac{t}{q_e} \ , \tag{6}$$

Where q is the CO_2 adsorption capacity of the adsorbent at time t (mmol·g^{-1}), q_e is the saturated CO_2 adsorption capacity in mmol·g^{-1}, k_1 is the fitting first-order kinetic constant in min^{-1}, and k_2 is a pseudo-second-order kinetic constant in g·mmol·$^{-1}$·min^{-1}.

Table S5 Kinetics parameters of adsorption of 400 pm CO_2 by NaX and PC60-NaX.

Kinetics model	Parameters	NaX	PC60-NaX
Pseudo-first-order kinetics	q_e	6.21	6.34
	k_1	0.28	0.36
	R^2	0.93	0.93
Pseudo-second-order kinetics	q_e	9.52	9.18
	k_2	0.020	0.029
	R^2	0.92	0.92

Table S6 Kinetics parameters of adsorption of 400 pm CO_2 and RH40 % water vapor by NaX and PC60-NaX.

Kinetic model	Parameters	NaX	PC60-NaX
Pseudo-first-order kinetics	q_e	123.90	748.86
	k_1	0.006	0.0039
	R^2	0.95	0.97

Adsorption heat

The classical method of obtaining adsorption heat data is based on the Clausius-Clapeyron equation, a series of isothermal adsorption data (at least two adsorption data at different temperatures) are used to obtain the calculation:

$$q^{st} = RT^2 \left[\frac{\delta \ln p}{\ln T}\right]_{n,s,A} = \Delta_a H. \quad (7)$$

q^{st} can be obtained from equation (7) by calculating the equivalent heat of adsorption by the adsorption isotherm:

$$\ln(\frac{p_1}{p_2}) = \frac{q^{st}}{R}\left[\left(\frac{1}{T_2} - \frac{1}{T_1}\right)\right], \quad (8)$$

Where p is the equilibrium absolute pressure (Pa), T is the adsorption temperature (K), R is the gas constant (0.00831kJ·mol^{-1}·k), and qst is the equivalent adsorption heat (kJ·mol^{-1}).

Table S7 The logarithm of the equilibrium constant lnK and Gibbs free energy ΔG^0 of CO_2 adsorption by NaX at different temperatures.

T		288K	298K	308K
ΔG^0	NaX	-22.46	-22.01	-21.66
	PC60-NaX	-26.77	-26.54	-26.69
ln*K*	NaX	4.69	4.44	4.21
	PC60-NaX	6.01	5.92	5.75

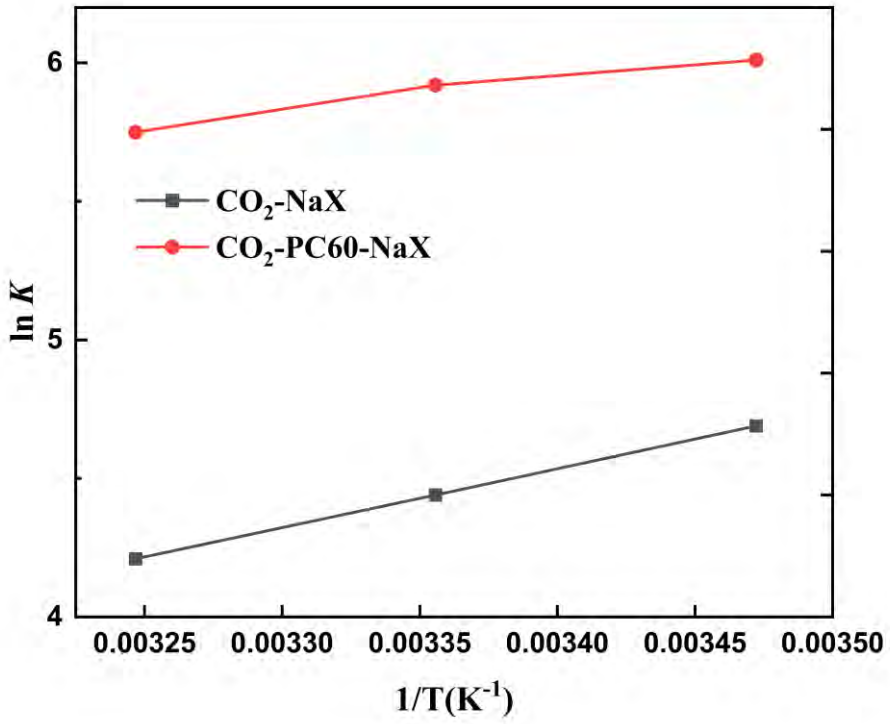

Figure S8. Van't Hoff plot for estimation of isosteric heat of CO_2 adsorption.

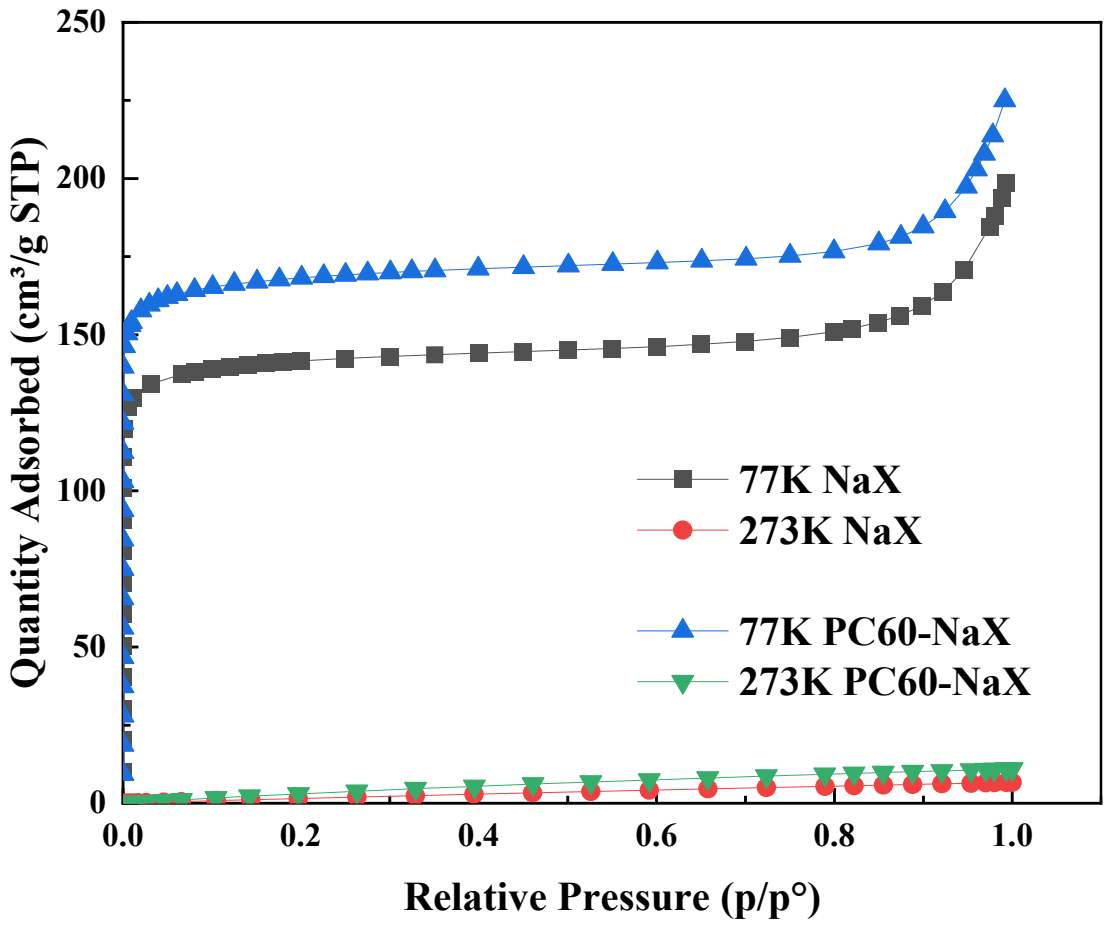

Figure S9. Adsorption isotherms of N_2 by NaX and PC60-NaX at 77 K and 273 K.

Table S8. Comparison of the adsorption properties of different adsorbents.

Sorbents	Temperature (℃)	Gas Composition	Capacity (mmol·g^{-1})	Refs.
PPI-SBA-15	35	400 ppm, dry	1.35	[8]
TEPA-$Mg_{0.55}$Al-O	25	400 ppm, dry	3.0	[9]
TREN-MIL-101(Cr)	25	400 ppm, dry	2.76	[10]
NaX	40	15-Iso[a]	3.38	[11]
Na-A	40	15-Iso[a]	1.40	[11]
Mg-A	40	15-Iso[a]	1.80	[11]
Ca-A	40	15-Iso[a]	3.81	[11]
HKUST-1	30	0.15 atm	1.59	[12]
Mg-MOF-74	30	0.15 atm	5.34	[12]
Zeolite 13X	30	0.15 atm	3.18	[12]
TEPA-SBA-15	30	0.15 atm	3.45	[12]
NaX (Original)	40	400 ppm, dry	4.92	This work
NaX-plasma-CO_2	40	400 ppm, dry	5.49	This work
3A (Original)	40	400 ppm, dry	5.11	This work
3A- plasma-CO_2	40	400 ppm, dry	5.50	This work
5A (Original)	40	400 ppm, dry	4.07	This work
5A-plasma-CO_2	40	400 ppm, dry	4.24	This work

[a] Data from isotherms and binary gas experiments; PPI: Poly(propylene imine); TEPA: Tetraethylenepentamine; TREN: Tris(2-aminoethyl)amine

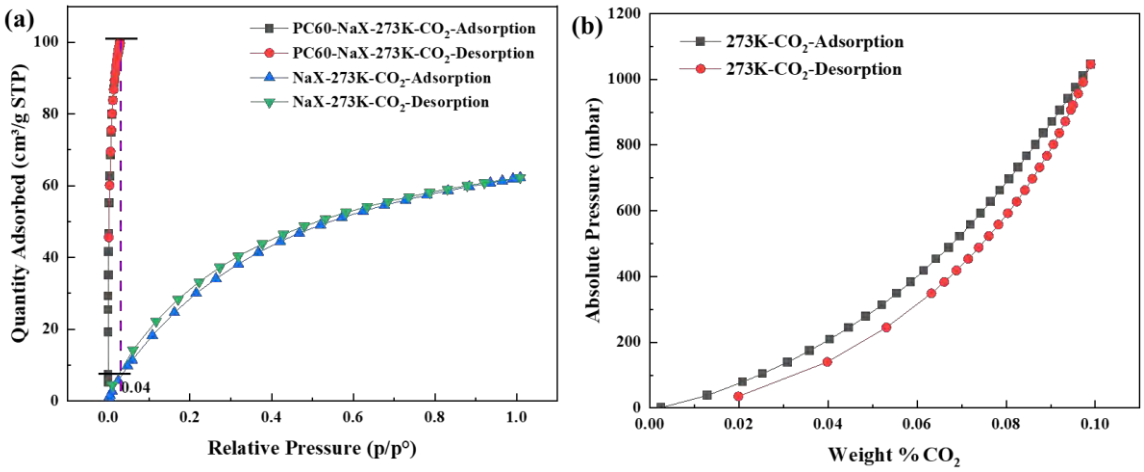

Figure S10. (a) CO_2 adsorption isotherms of NaX and PC60-NaX at 273 K and (b) Adsorption isotherms of PC60-NaX for different CO_2 mass fractions at 273K.

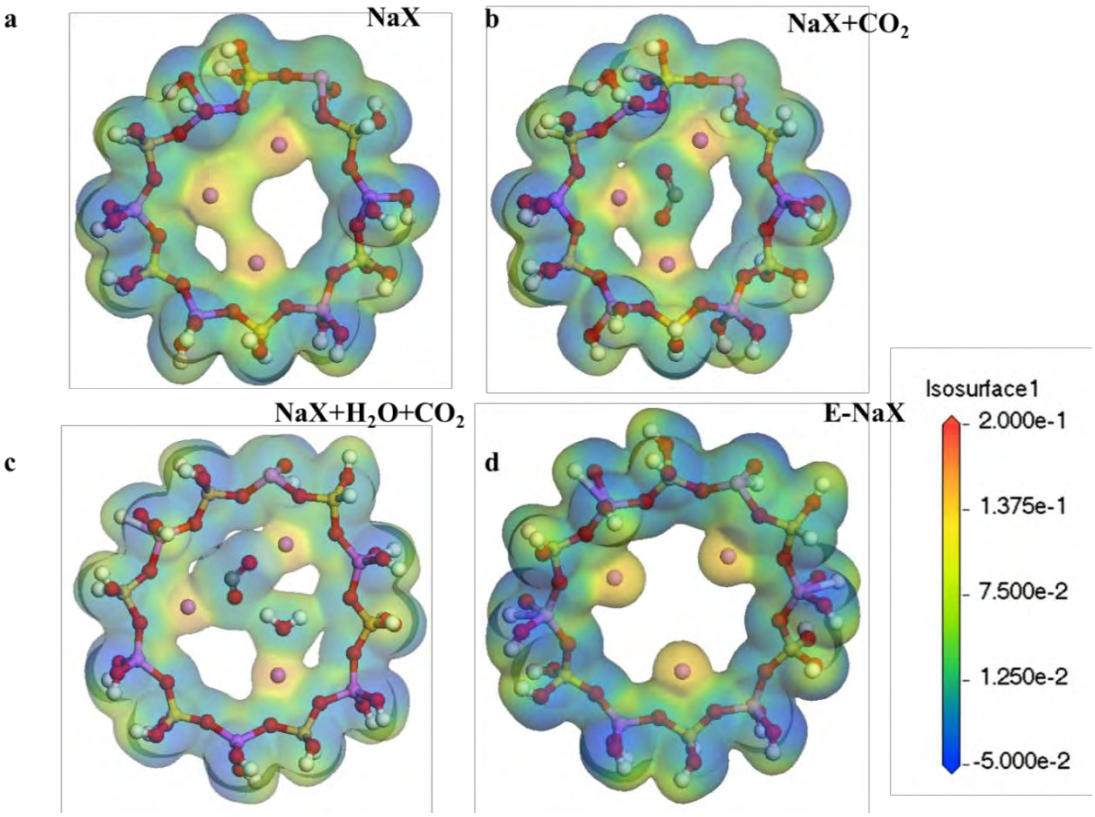

Figure S11. Surface electrostatic potential energy distributions of the twelve binary rings of NaX: (a) NaX, (b) NaX+CO_2, (c) NaX+CO_2+H_2O, and (d) NaX under the electric field.

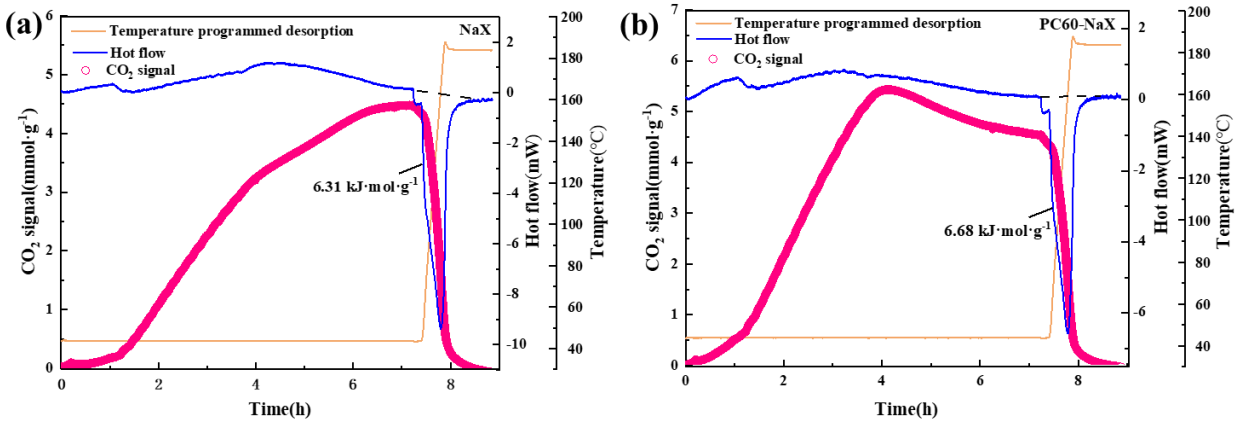

Figure S12. Desorption heat of NaX and PC60-NaX based on DSC.

TableS9 Multi-constituent adsorption Breakthrough of CO_2 and H_2O.

Composition	Parameter	Unit	Breakthrough Point (5%)		Half Dry Point (50%)		Dry Point (95%)	
			NaX	PC60-NaX	NaX	PC60-NaX	NaX	PC60-NaX
CO_2	Times	s	1154.8	2254.3	1287.4	2386.9	1521.3	2457.0
		s/g	1287.6	2634.5	1435.4	2789.4	1696.2	2871.4
	Outlet concentration	V/V%	0.002	0.002	0.021	0.021	0.038	0.039
	Outlet flow	ml/min (STP)	0.002	0.002	0.020	0.020	0.037	0.038
	Adsorption capacity	mmol/g	0.038	0.078	0.041	0.082	0.043	0.082
H_2O	Times	s	5942.6	6870.5	6192.1	7237.0	6605.4	7611.3
		s/g	6625.7	8029.1	6903.9	8457.4	7364.7	8894.8
	Outlet concentration	V/V%	0.141	0.147	1.408	1.449	2.676	2.677
	Outlet flow	ml/min (STP)	0.137	0.143	1.387	1.428	2.670	2.670
	Adsorption capacity	mmol/g	13.834	16.765	14.271	17.444	14.488	17.601

Explanations：

(1) Penetration point: the point on the penetration curve where the concentration of adsorbent gas at the exit of the penetration column reaches 5% of the inlet concentration (default)

(2) Semi-dry point: the point on the penetration curve where the concentration of adsorbent gas at the exit of the penetration column reaches 50% of the inlet concentration (default)

(3) Dry point: the point on the penetration curve where the concentration of adsorbent gas at the exit of the penetration column reaches 95% of the inlet concentration (default)

(4) Penetration adsorption capacity: the corresponding adsorption capacity of the adsorbent gas at the penetration point

(5) Dry point adsorption capacity: the corresponding adsorption capacity of the adsorbent gas at the dry point

(6) The horizontal coordinate of penetration point, semi-dry point and dry point is time, and the vertical coordinate is volume percentage concentration (STP).

(7) Saturated adsorption capacity: When the outlet concentration of the adsorbent gas is equal to the inlet concentration, the adsorption capacity of the adsorbent on the adsorbent gas

TableS10 Multicomponent adsorption diffusion coefficients of CO_2 and H_2O.

Samples	Composition	Outflow Time/s	Delay Time/s	Bed Thickness/cm	Diffusivity /(cm^2/s)
NaX	CO_2	1217.23	601.71	5.1	0.0072
	H_2O	5872.39	353.54	5.1	0.0123
PC60-NaX	CO_2	2316.69	709.77	4.7	0.0052
	H_2O	6745.72	464.74	4.7	0.0079

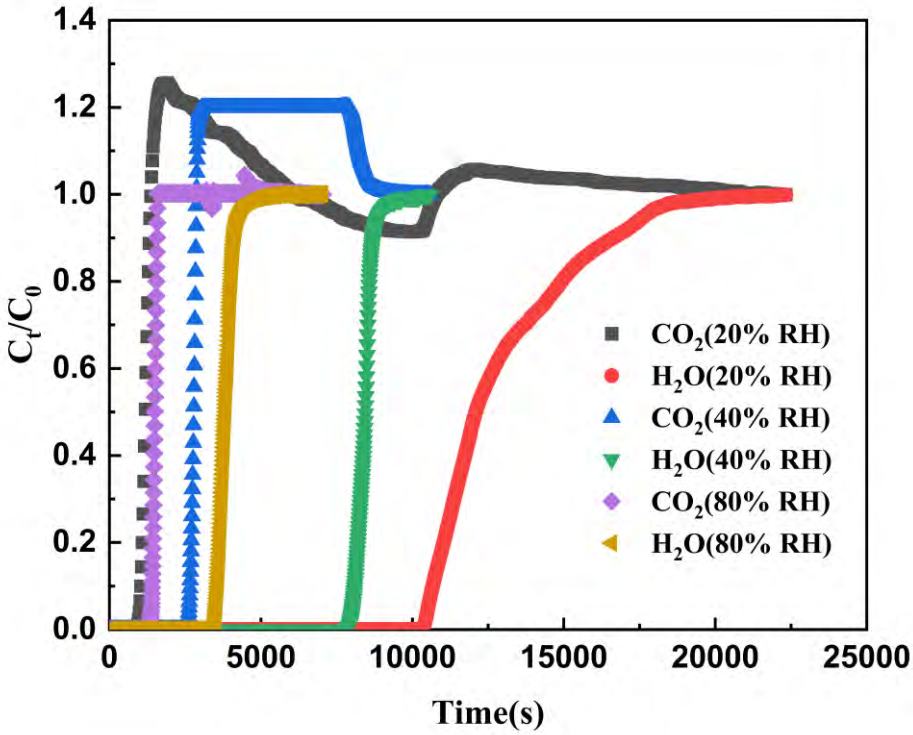

Figure S13. Adsorption breakthrough curves of CO_2 and H_2O on PC60-NaX under different humidity environments(C_t: Inlet concentration; C_0: Outlet concentration).

References

[1] S. U. Rege, R. T. Yang, Chem. Eng. Sci. 2001, 56, 3781-3796.

[2] J. Wang, X. Guo, Chemosphere 2020, 258, 127279.

[3] G. K. Rajahmundry, C. Garlapati, P. S. Kumar, R. S. Alwi, D.-V. N. Vo, Chemosphere 2021, 276, 130176.

[4] M. M. Majd, V. Kordzadeh-Kermani, V. Ghalandari, A. Askari, M. Sillanpää, Sci. Total Environ. 2022, 812, 151334.

[5] O. M. Adedeji, K. Jahan, Chemosphere 2023, 321, 138165.

[6] J. Serafin, B. Dziejarski, Microporous Mesoporous Mater. 2023, 354, 112513.

[7] M. A. Al-Ghouti, D. A. Da'ana, J. Hazard. Mater. 2020, 393, 122383.

[8] S. H. Pang, L.-C. Lee, M. A. Sakwa-Novak, R. P. Lively, C. W. Jones, J. Am. Chem. Soc. 2017, 139, 3627-3630.

[9] M. Zhao, J. Xiao, W. Gao, Q. Wang, J. Energy Chem. 2022, 68, 401-410.

[10] L. A. Darunte, A. D. Oetomo, K. S. Walton, D. S. Sholl, C. W. Jones, ACS Sustainable Chem. Eng. 2016, 4, 5761-5768.
[11] T.-H. Bae, M. R. Hudson, J. A. Mason, W. L. Queen, J. J. Dutton, K. Sumida, K. J. Micklash, S. S. Kaye, C. M. Brown, J. R. Long, Energy Environ. Sci. 2013, 6, 128-138.
[12] A. Kumar, D. G. Madden, M. Lusi, K. J. Chen, E. A. Daniels, T. Curtin, J. J. Perry IV, M. J. Zaworotko, Angewandte Chemie International Edition 2015, 54, 14372-14377.